The Astrophysical Journal, 986:173 (19pp), 2025 June 20 https://doi.org/10.3847/1538-4357/adabde

Quantum Plasma Creation near a Magnetar

Jonathan Zhang[1] and Christopher Thompson[2]
[1] Department of Physics, McLennan Physical Labs, Toronto, ON M5S 1A7, Canada; jzhang@physics.utoronto.ca
[2] Canadian Institute for Theoretical Astrophysics, 60 St. George Street, Toronto, ON M5S 3H8, Canada
Received 2024 July 11; revised 2025 January 10; accepted 2025 January 16; published 2025 June 20

Abstract

Magnetars in quiescent states continue to emit hard X-rays with a power far exceeding the loss of rotational energy. It has recently been noted that this hard X-ray continuum may bear a direct signature of quantum electrodynamic effects in magnetic fields stronger than the Schwinger field ($B_{\rm Q} = 4.4 \times 10^{13}$ G). Where the current flowing into the magnetosphere is driven by narrow structures in the solid crust, the $e^{\pm}$ pair plasma supporting the current relaxes to a collisional and transrelativistic state. The decay of a pair into two photons produces a broad, bremsstrahlung-like spectrum of hard X-rays, similar to that observed and extending up to 0.5−1 MeV. The conversion of two gamma-rays to a pair is further enhanced by a factor $\sim B/B_{\rm Q}$. Monte Carlo calculations of pair creation in a dipole magnetic field are presented. Nonlocal particle injection is found to be strong enough to suppress the high voltage that otherwise would accompany a weaker, global twist; the hard X-rays are mostly emitted away from the magnetic poles. Some of the pairs annihilate in an optically thin surface layer. The prototypical anomalous X-ray pulsar 1E 2259+586, which shows a hard X-ray continuum but relatively weak torque noise, slow spindown, and no radio emission, is a Rosetta Stone for understanding the magnetar circuit, consistent with the picture advanced here. For a 15−60 keV luminosity as low as 10^{34} erg s^{-1}, the polar flux of subrelativistic pairs produces an optical depth of 3−30 to electron cyclotron scattering in the 1−10 keV band, reducing the net X-ray polarization.

Unified Astronomy Thesaurus concepts: Cosmic electrodynamics (318); Gamma-rays (637); Magnetars (992); Magnetic fields (994); Non-thermal radiation sources (1119); Plasma astrophysics (1261)

1. Introduction

Magnetars are sources of electromagnetic outbursts that are bright enough to be detectable outside the Milky Way, as gamma-ray transients and radio bursts (C. D. Bochenek et al. 2020; CHIME/FRB Collaboration et al. 2020; E. Burns et al. 2021). In contrast with core-collapse-driven explosions (supernovae and jet-driven gamma-ray bursts), the early stages of outbursts can be closely monitored in nearby Galactic sources (V. M. Kaspi & A. M. Beloborodov 2017).

The broadband radiative emissions of magnetars are mostly powered by the decay of nonpotential magnetic fields and supporting $\sim 10^{20}$ A currents. In contrast with rotation-powered pulsars, the currents flowing outside the star may approach in strength those flowing in the interior (C. Thompson et al. 2002; M. Lyutikov 2006; A. M. Beloborodov & C. Thompson 2007; C. Thompson 2008b; A. M. Beloborodov 2009; K. Parfrey et al. 2012; A. Y. Chen & A. M. Beloborodov 2017; C. Thompson & A. Kostenko 2020; J. F. Mahlmann et al. 2023).

Important clues are provided by the broad and spectrally hard X-ray continuum that dominates the bolometric output of the brightest quiescent magnetars above 10−20 keV (D. Götz et al. 2006; L. Kuiper et al. 2006; T. Enoto et al. 2017, and references therein). The X-ray power can reach $\sim 10^3$ times the spindown power, and therefore cannot be explained by the standard pulsar model.

Magnetar X-ray emission carries a direct imprint of quantum electrodynamic (QED) processes in magnetic fields stronger than the Schwinger field, as normalized by the electron rest mass ($B_{\rm Q} = m_e^2 c^3/e\hbar = 4.4 \times 10^{13}$ G). In this regime, all basic interactions of electrons, positrons, and photons are altered qualitatively: binary collisions are significantly enhanced and nonlinear effects become directly testable (S. L. Adler 1971; J. K. Daugherty & R. W. Bussard 1980; A. A. Kozlenkov & I. G. Mitrofanov 1986; P. L. Gonthier et al. 2014; A. Kostenko & C. Thompson 2018, 2019).

Collisional $e^{\pm}$ plasma in super-QED magnetic fields offers a economical explanation for the measured hard X-ray continuum. The annihilation of transrelativistic $e^{\pm}$ pairs via $e^+ + e^- \rightarrow \gamma + \gamma$ generates a broad, bremsstrahlung-like spectrum in magnetic fields stronger than $\sim 4\,B_{\rm Q} \sim 2 \times 10^{14}$ G (A. Kostenko & C. Thompson 2018). The emission spectrum can be modified, most readily around the peak, by reabsorption by photon collisions and multiple electron scattering. These effects are included in the QED Monte Carlo (MC) simulations of C. Thompson & A. Kostenko (2020). That work is extended here to consider the nonlocal effects of gamma-ray collisions.

In this approach, we uncover a direct connection between the hard spectral component observed in quiescent magnetars and the bi-refringent properties of the magnetized vacuum. Hard X-rays only escape the inner magnetosphere in the ordinary mode (O-mode): the extraordinary mode (E-mode or X-mode) rapidly splits into two O-mode photons, E → O + O, above an energy ~ 40 keV (S. L. Adler 1971; C. Thompson & R. C. Duncan 1995).

Understanding the mechanism of hard X-ray emission is an essential step toward a self-consistent description of magnetar electrodynamics. There are important implications for X-ray polarization (R. Taverna et al. 2022; R. Turolla et al. 2023; J. Heyl et al. 2024; M. Rigoselli et al. 2025), peculiar pulsed radio emission (F. Camilo et al. 2006, 2007; L. Levin et al. 2010),

and the mechanism by which the solid crust of the magnetar transmits magnetic stresses to its exterior.

Even while hard X-ray emission and rapid spindown in magnetars are generally correlated, their time profiles in individual sources can be strongly decorrelated: torque increases and radio emission will frequently lag peak X-ray flux by months to years (e.g., R. F. Archibald et al. 2015). The currents driving the bolometric output of a quiescent magnetar may not in many cases be concentrated close to the magnetic poles—an interesting clue as to why the fast radio burst (FRB) phenomenon appears rare in Galactic magnetars (E. Petroff et al. 2022).

1.1. Nonlocal $\gamma-\gamma$ Pair Creation

In this paper, we use an MC method to evaluate the global distribution of pairs created by γ - γ collisions. The pair creation rate is sensitive to details of the source spectrum around photon energy $m_e c^2$. The quiescent hard X-ray continuum is observed to rise in energy flux up to $\sim$100 keV (D. Götz et al. 2006; P. R. den Hartog et al. 2008a, 2008b; T. Enoto et al. 2017). There is no sign of a cutoff below 100 keV, although earlier, noncontemporaneous COMPTEL measurements are suggestive of a cutoff above 1 MeV in three sources (L. Kuiper et al. 2006). For comparison, the spectrum emitted by a transrelativistic and collisional $e^{\pm}$ plasma is predicted to extend to $\sim 0.5-1$ MeV, but then cut off hyper-exponentially above $\sim m_e c^2$ (C. Thompson & A. Kostenko 2020).

In super-QED magnetic fields, the collision of gamma-rays is significantly enhanced: the cross section increases by a factor $\sim B/B_{\rm Q}$ compared with vacuum and the kinematic constraints on photon collisions are also relaxed (A. A. Kozlenkov & I. G. Mitrofanov 1986; A. Kostenko & C. Thompson 2018). The measured X-ray output at $\sim$50 keV, extrapolated upward in energy, implies a total $e^{\pm}$ annihilation luminosity reaching $\sim 10^{35}$ or 10^{36} erg s^{-1} and a significant optical depth to photon collisions.

1.2. Self-consistent Circuit State

More than one self-consistent state is available to the $e^{\pm}$ plasma supplying the current, potentially leading to large variations in voltage and temporal behavior. When the current density is not too high throughout the magnetosphere, a double layer structure forms. Electron–positron pairs are self-consistently generated via scattering of kiloelectronvolt surface photons at the electron Landau resonance, the embedded charges reaching a Lorentz factor $\sim 10^{2-3}$ (A. M. Beloborodov & C. Thompson 2007).

More recently, it has been recognized that stronger (and more localized) currents can relax to a collisional and transrelativistic plasma state (C. Thompson & A. Kostenko 2020). The $e^{\pm}$ interact repeatedly through the one- and two-photon annihilation channels. Energy and annihilation equilibrium are reached when the particle density is larger by a factor $\sim$15 than the minimum needed to support the background magnetic shear.

These distinct circuit configurations are not fully compatible, and have differing implications for the source of the hard X-ray continuum. The magnetic twist could be concentrated around the magnetic poles and supported by outward streaming e^{+} and e^{-} (A. M. Beloborodov 2009, 2013a). By contrast, denser plasma structures ("twist zones") that connect to crustal shear bands would be distributed more broadly over the magnetar surface (C. Thompson et al. 2017). We consider the complementary case where the dominant dissipative structures are anchored at magnetic latitudes around 45°.

The gamma-rays emitted from collisional plasma will reach much (but not necessarily all) of the magnetosphere. As we show here, the pairs produced nonlocally by secondary gamma-ray collisions can easily short out the high-voltage, double-layer structure.

Weaker currents flowing into the outer magnetosphere can, in particular, be sustained by this injection of pairs. The polar region of a magnetar is of interest for several reasons. During limited phases of activity, this zone appears to support enhanced magnetic twist that drives large variations in spindown torque and pulsed radio emission (R. F. Archibald et al. 2015), and may also on occasion emit FRBs (B. Zhang 2023). Scattering of $1-10$ keV photons at the electron cyclotron resonance also has a significant effect on X-ray pulse profiles (R. Fernández & C. Thompson 2007; L. Nobili et al. 2008).

1.3. 1E 2259+586 as a Test Case

The prototypical anomalous X-ray pulsar 1E 2259+586 (G. G. Fahlman & P. C. Gregory 1981) offers some relatively clean tests of magnetar electrodynamics. Its X-ray spectrum should be less modified by repeated scattering than in other magnetars with stronger external currents and higher luminosities above 100 keV. The polar dipole field inferred from spindown is also weak enough (about 1.2×10^{14} G) to imply measurable deviations from the bremsstrahlung-like spectrum that is expected from $e^{\pm}$ annihilation in magnetic fields approaching 10^{15} G.

In fact, 1E 2259+586 has one of the hardest $20-50$ keV spectra detected in quiescent magnetars (J. K. Vogel et al. 2014), consistent with pair annihilation in a magnetic field near $B_{\rm Q}$ (see Figure 3 of C. Thompson & A. Kostenko 2020). It is correspondingly dimmer at 20 keV than more burst-active magnetars with stronger magnetic fields and flatter high-energy spectra (the soft gamma repeaters or SGRs).

The hard X-ray flux emitted by 1E 2259+586 (and extrapolated to $\sim 0.5-1$ MeV) implies a modest optical depth to gamma-ray collisions in the bulk of the magnetosphere. A first-order MC analysis therefore can be carried out by neglecting the effects of multiple scattering, which are left to future work.

At the same time, 1E 2259+586 has a relatively quiet spindown history and a characteristic age much greater than the age of the surrounding supernova remnant CTB 109 (R. Dib & V. M. Kaspi 2014). Pulsed radio emission has never been detected (e.g., M. J. Coe et al. 1994). 1E 2259+586 therefore has an ensemble of properties consistent with the proposition that the source of the hard X-ray continuum can be separated spatially in a magnetar from the polar magnetic field bundle that controls spindown torque and radio emission—in contrast with the approach described by R. Fernández & C. Thompson (2007), M. G. Baring & A. K. Harding (2007), and A. M. Beloborodov (2013a).

Finally, 1E 2259+586 shows persistent infrared emission $\sim 10^2$ times brighter than is expected from the Rayleigh–Jeans tail of the surface 0.4 keV blackbody (F. Hulleman et al. 2001). Strong coherent plasma emission in the optical-IR band, which is observed more frequently than pulsed radio emission, is also a natural consequence of a collisional plasma state with high

density (D. Eichler et al. 2002; C. Thompson & A. Kostenko 2020).

1.4. Plan of the Paper

Section 2 reviews the interactions of electrons, positrons, and photons in super-QED magnetic fields, with a focus on enhanced rates of pair creation and the formation of a collisional plasma state. The magnetospheric configurations that are adopted as backgrounds for our MC calculations of $\gamma - \gamma$ pair creation are described in Section 3, and the gravitational lensing of gamma-rays is described in Section 4. Our MC method is detailed in Section 5, and results are presented in Section 6. We summarize the broader implications of our calculations for the torque behavior, electromagnetic spectra, and pulse structure of magnetars in Section 7.

Throughout this paper, we use standard notation for electron rest mass m_e, magnitude of the electron charge e, speed of light c, reduced Planck constant $\hbar$, and Newton's constant G. The numerical value of quantity X is normalized as $X = X_n \times 10^n$ in cgs units.

2. QED Processes and the Magnetar Plasma State

The plasma state outside an active magnetar is sensitive to details of the interactions between electrons, positrons, and photons in a super-QED magnetic field. Here, we describe the enhancement of (i) electron–positron collisions in zones of high current density and (ii) gamma-ray collisions throughout the rest of the magnetosphere. We then show how compensating losses of pairs determine the equilibrium pair density.

2.1. Enhanced Resistivity from Pair Annihilation

Dissipation outside a neutron star (NS) of radius $R_{\rm NS} \sim 10$ km at a rate $L_X \sim 10^{35}-10^{36}$ erg s^{-1} would not ordinarily sustain optically thick pair plasma: the radiative compactness defined in terms of the nonmagnetic Thomson cross section is $\sigma_{\rm T} L_X/4\pi m_e c^3 R_{\rm NS} \lesssim 1$. However, in a super-QED magnetic field, two quantum effects allow for a pair plasma to settle into a collisional and transrelativistic state.

First, as in radio pulsars, the annihilation of a pair into a single photon, $e^+ + e^- \rightarrow \gamma$, is allowed by the conservation of canonical momentum $\boldsymbol{p} \pm e\boldsymbol{A}/c$, where $\boldsymbol{A}$ is the vector potential associated with the stellar magnetic field. This process is resonant, with a cross section exceeding $\sigma_{\rm T}$ by a factor $\sim(\alpha_{\rm em} B/B_{\rm Q})^{-1}$, where $\alpha_{\rm em} \simeq 1/137$ is the fine structure constant (G. Wunner 1979):

$$\sigma_{\rm ann,1\gamma} = \frac{3\pi}{4\beta\gamma^2\alpha_{\rm em}(B/B_{\rm Q})}\sigma_{\rm T}. \quad (1)$$

Here, βc and γ are the center-of-momentum (COM) speed and Lorentz factor of the $e^{\pm}$. The created photon will almost immediately convert back to a pair, over a microscopic distance. Half the time, the momenta of the regenerated electron and positron are reversed, producing a backscattering.

The second effect enhancing the pair density involves a suppression of radiative cooling. Two-photon annihilation of the pairs, $e^+ + e^- \rightarrow \gamma + \gamma$, is suppressed by a factor $\sim(B/B_{\rm Q})^{-1}$. This means that the equilibrium particle density needed to balance ohmic heating by backscattering is larger, by a factor $f_n \equiv (n_{e^+} + n_{e^-})/n_{\rm crit} \sim 15$, than the minimum density $2n_{\rm crit} = |\nabla \times \boldsymbol{B}|/4\pi\beta e$ that will support a static magnetic twist (C. Thompson & A. Kostenko 2020). In addition, in super-QED magnetic fields, most of the energy released in two-photon annihilation is carried by a single photon. This energetic photon frequently reconverts to a pair, so that only a fraction of the total energy is lost to an "annihilation bremsstrahlung" photon.

A third effect reducing energy loss by transrelativistic pairs is the appearance of a strong u-channel resonance in the cross section for $\gamma - e^{\pm}$ scattering (A. Kostenko & C. Thompson 2018). This resonance is encountered when the photon energy approaches the threshold for single-photon pair conversion, $\hbar\omega \lesssim \hbar\omega_{1\gamma} \equiv 2m_e c^2/\sin\theta_{kB}$. (Here, $\theta_{kB} = \cos^{-1}(\hat{k}\cdot\hat{B})$ is the angle of propagation of a photon of wavevector $\boldsymbol{k} = k\hat{k}$ with respect to the local magnetic field $\boldsymbol{B}$.)

The net effect is that collisional pair plasma can be sustained in a quiescent magnetar in narrow flux elements sustaining strong magnetic shear. Given a shear length $\ell_B = B/|\nabla \times \boldsymbol{B}|$ and pair density $n_p = n_{e^+} = n_{e^-}$, the normalized optical depth for e^+ to backscatter off e^- along a length $\ell_\parallel$ of a magnetic arcade is

$$\frac{\sigma_{\rm ann,1\gamma}}{2} n_p\, \ell_\parallel \sim \frac{\pi}{8\beta^2\gamma^2}\left(\frac{n_p}{n_{\rm crit}}\right)\frac{\ell_\parallel}{\ell_B} = 10\left(\frac{f_n}{15}\right)\frac{\ell_\parallel}{\ell_B} \qquad (\beta \sim 0.6). \quad (2)$$

Small-scale braiding of the magnetic field, with an amplitude $\delta B < B$, wavenumber $k_\perp \gg R_{\rm NS}^{-1}$, and twist density $k_\perp \delta B \gg B/R_{\rm NS}$, will further enhance the current density and collision rate. In this way, the appearance of collisional plasma outside a quiescent magnetar is diagnostic of the yielding motions that are driven by Maxwell stresses operating below the stellar surface.

Magnetar outbursts point to crustal dissipation with the required properties: fault-like zones of subkilometer width that locally shear the magnetic field. Most bright SGR bursts have a duration $\sim$0.1 s, comparable to the time for elastic stresses to propagate around the star (E. Göğüş et al. 2001). They are often followed by decaying hotspot emission covering a few percent or less of the magnetar surface (V. M. Kaspi & A. M. Beloborodov 2017). Pseudofaults with this property are observed in a global elastic-plastic-thermal model of the thin[3] crustal shell (C. Thompson et al. 2017).

Details of the transition from a double-layer plasma structure at low current density to a collisional state at high current density remain to be investigated. Such a transition is expected because (i) the double layer structure is much more dissipative at high current density; (ii) the photon flux resulting from particle bombardment of the magnetar surface by relativistic $e^{\pm}$ will greatly enhance nonresonant photon–electron drag, leading to runaway growth in photon energy density when $n_{\rm crit}\sigma_{\rm T} R_{\rm NS} > 1$; and (iii) a magnetar may produce collisional plasma during a bright, transient outburst, which is accompanied by hysteresis in the collision rate as the luminosity drops.

2.2. Photon Interactions and Enhanced Collisions

Because we are considering dissipative zones with a limited scattering depth ($\lesssim$3–10), our focus is on the emission, propagation, and absorption of the ordinary polarization mode

[3] The thickness of the NS crust weighted by the depth-dependent shear modulus is typically $\sim$0.3 km.

(O-mode). The effect of the background magnetic field on photon–electron interactions can be understood semiclassically in terms of a suppression of $\boldsymbol{E} \times \boldsymbol{B}$ drift of the electron. The O-mode has electric vector partly overlapping the background magnetic field: $\delta\boldsymbol{E} \propto \hat{k} \times (\hat{k} \times \boldsymbol{B})$ when the photon propagates in direction $\hat{k}$. The interactions of the E-mode are suppressed by factors $\sim(\omega m_e c/eB)^2$ at frequency ω (A. K. Harding & D. Lai 2006). The cross sections calculated by A. Kostenko & C. Thompson (2018, 2019) in super-QED magnetic fields are restricted to the O-mode.

Fundamental to our considerations is the inability of O-mode X-rays to split, $\gamma \rightarrow \gamma + \gamma$, in the energy range $\hbar\omega \gtrsim 40$ keV where the E-mode is rapidly absorbed (S. L. Adler 1971). The strongly magnetized zone around pulsars or magnetars has bi-refringent properties deriving from the nonlinearity in Maxwell's equations that is imparted by vacuum polarization. The correction to the O-mode index of refraction kc/ω from vacuum polarization is of the order of $\alpha_{\rm em}B/B_{\rm Q}$ in super-QED magnetic fields, whereas the E-mode only receives a correction of the order of $\alpha_{\rm em}$. This means that energy and momentum can be conserved in the splitting of a photon into two obliquely propagating photons only when at least one daughter photon has the larger index of refraction. The strong break seen around 10−20 keV in many quiescent magnetar spectra may be directly related to this QED effect, if the lower-energy kiloelectronvolt surface emission is partly carried by the E-mode.

Let us consider the ensemble of O-mode photons that are below the threshold for direct conversion to an electron–positron pair, $\omega < \omega_{1\gamma}$. (This energy depends on the local angle of propagation θ_{kB} with respect to $\boldsymbol{B}$, meaning that even if $\omega < \omega_{1\gamma}$ at emission, one must repeatedly check for absorption along a ray trajectory.) The volumetric rate of two-photon pair creation is given in terms of the cross section σ by

$$\dot{n}_{\gamma\gamma\rightarrow e^+e^-} = \int d\hat{k}_1 d\hat{k}_2 d\omega_1 d\omega_2 \left[\frac{d^2n_{\gamma 1}}{d\hat{k}_1 d\omega_1}\frac{d^2n_{\gamma 2}}{d\hat{k}_2 d\omega_2} \times |1-\mu_{12}| c\,\sigma(\omega_1, \omega_2, \hat{k}_1, \hat{k}_2, B)\right]. \quad (3)$$

Here, n_γ is the photon density, which must be evaluated at each position over a range of momenta of photons 1 and 2, and $\mu_{12} = \hat{k}_1 \cdot \hat{k}_2$.

The kinematic constraints on $\gamma + \gamma \rightarrow e^+ + e^-$ are relaxed in a super-QED magnetic field. In vacuum, the energies of the two photons must pass the threshold

$$C_{+,B=0} \equiv 2\hbar\omega_1\,\hbar\omega_2(1-\mu_{12}) > 4m_e^2c^4. \quad (4)$$

A soft photon of energy $\hbar\omega_s \ll m_e c^2$ may convert to a pair by colliding with a much harder photon of energy $\hbar\omega \gtrsim (m_e c^2)^2/\hbar\omega_s \gg m_e c^2$. When $B \gtrsim B_{\rm Q}$, the same soft photon can collide with a photon that individually is not much below the threshold energy $\hbar\omega_{1\gamma} \sim 2m_e c^2$ in the COM frame. Pair conversion only requires

$$C_+ \equiv (\hbar\omega_1 + \hbar\omega_2)^2 - (\mu_1\hbar\omega_1 + \mu_2\hbar\omega_2)^2 > 4m_e^2c^4, \quad (5)$$

where $\mu_i = \hat{k}_i \cdot \hat{B}$. Note also that two colinear photons can now convert to a pair, as a result of the breakdown in the conservation of kinetic momentum perpendicular to $\boldsymbol{B}$.

The cross section for $\gamma + \gamma \rightarrow e^+ + e^-$ in magnetic fields stronger than $\sim 4B_{\rm Q}$ can be written for arbitrary photon frequencies and direction cosines (not satisfying the COM condition $\omega_1\mu_1 = -\omega_2\mu_2$) as (A. Kostenko & C. Thompson 2018; see Equation (7) of Erratum),

$$\sigma_{\gamma\gamma}[B \gg B_{\rm Q}] = \frac{32\pi r_e^2}{|1-\mu_{12}|}\frac{B}{B_{\rm Q}}\frac{\sqrt{C_+ - 4m_e^2c^4}}{C_+^{1/2}(\hbar^2\omega_1\omega_2)^3} \times \frac{C_+^2(1-\mu_1^2)(1-\mu_2^2)(m_e c^2)^6}{[C_+(1-\mu_1^2)(1-\mu_2^2) + 4m_e^2c^4(\mu_1-\mu_2)^2]^2}. \quad (6)$$

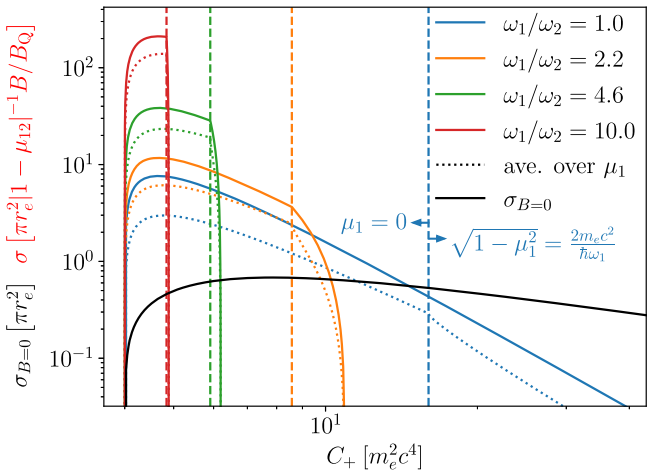

Figure 1. Cross section for $\gamma + \gamma \rightarrow e^+ + e^-$. Colored lines: the regime $B \gtrsim 4B_{\rm Q}$, plotted as a function of $C_+ = (\hbar\omega_1 + \hbar\omega_2)^2 - (\mu_1\hbar\omega_1 + \mu_2\hbar\omega_2)^2$, for various ratios ω_1/ω_2 of photon energies. Solid lines: cross section at the lowest value of $\mu_1 = \hat{k}_1 \cdot \hat{B}$ consistent with $\omega_1 < \omega_{1\gamma} = 2m_e c^2/\hbar(1-\mu_1^2)^{1/2}$; this is $\mu_1 = 0$ to the left of the vertical dashed line, and $\mu_1 > 0$ to the right. Dotted line: average over all μ_1 for which $\omega_1 < \omega_{1\gamma}$. Black curve: cross section in vanishing magnetic field, now with $C_+ = 2\hbar\omega_1\hbar\omega_2(1-\mu_{12})$.

One sees from Figure 1 that collisions between soft and hard photons have a higher cross section than collisions between photons with comparable energy.

The enhancement in $\sigma_{\gamma\gamma}$ by a factor $\sim B/B_{\rm Q}$ is readily seen to be a consequence of annihilation-creation equilibrium: the cross section for the reverse $e^\pm$ annihilation process is suppressed by a factor $\sim(B/B_{\rm Q})^{-1}$. A simple case is a thermal pair gas with a temperature $\lesssim m_e c^2$ and a density $\propto B/B_{\rm Q}$, this factor arising from the phase space volume in the plane perpendicular to $\boldsymbol{B}$.

The magnetic field is weaker at greater distances from the magnetar, and we adopt the nonmagnetic cross section where $B < B_{\rm Q}$. Selecting out a single polarization state (that is, the O-mode), one has (G. Breit & J. A. Wheeler 1934):

$$\sigma_{\gamma\gamma}[B=0] = \pi r_e^2\left[-SC^{-3} - \tfrac{3}{2}SC^{-5} - \tfrac{3}{2}\theta C^{-6} + 2\theta C^{-4} + 2\theta C^{-2}\right]. \quad (7)$$

Here, $\{S, C\} = \{\sinh\theta, \cosh\theta\}$ and the COM photon energy is parameterized as $[(1-\mu_{12})/2]^{1/2}\hbar(\omega_1\omega_2)^{1/2} = m_e c^2\cosh\theta$. Most of the pairs are created in the inner part of the magnetosphere where $B > B_{\rm Q}$; we do not represent the complicated transition between the two limiting expressions for $\sigma_{\gamma\gamma}$.

2.3. Compensating Loss of Pairs

The production of pairs outside the gamma-ray emitting twist zones is compensated for by (i) volumetric annihilation

and (ii) loss through the surface of the star. In addition, (iii) pairs are preferentially pushed away from the star on polar field lines, where the outward pressure of kiloelectronvolt photons acting at the electron cyclotron resonance provides a strong barrier to inward motion beyond a radius $(15-30)\,R_{\rm NS}$ (C. Thompson 2008a; A. M. Beloborodov 2013b). Radiation pressure from the heated surface does not limit the impact and annihilation of positrons, at least when the radiation intensity is low enough that only a fraction of gamma-rays experience collisions.

The pair density n_p we obtain is much larger than the corotation density $n_c = |\Omega \cdot \boldsymbol{B}|/2\pi ec$ when the rotation period is larger than 1 s, as typically observed in magnetars. As a result, the plasma is locally charge balanced, $n_{e^+} \simeq n_{e^-}$.

2.3.1. Volumetric Annihilation

In the idealized case of local kinetic equilibrium, there is a simple relation between the densities of pairs and gamma-rays. Annihilation into a single photon leads immediately to regeneration of the pair. Some fraction of the time, the same is true for annihilation into two photons, through the process of annihilation bremsstrahlung $e^+ + e^- \rightarrow \gamma + \gamma \rightarrow \gamma + e^+ + e^-$. The cross section to annihilate into two photons, both of which are below threshold for direct pair conversion ($\omega < \omega_{1\gamma}$) is (C. Thompson & A. Kostenko 2020)

$$\sigma_{\rm ann,2\gamma}[B > B_{\rm Q}] = \frac{8\pi r_e^2}{B/B_{\rm Q}}\frac{\beta}{\gamma^2}\left[\frac{5}{9} - 1.29\beta^2 - 0.0886\beta^4 - \ln(\beta)\left(\frac{4}{3} + 0.936\beta^2 + 4.54\beta^4\right)\right]. \quad (8)$$

Balancing the rate of pair creation by two photons of comparable energy with annihilation of $e^{\pm}$ with kinetic energy $\hbar\omega - m_e c^2$ gives

$$\frac{n_p}{n_\gamma} = \left(\frac{|1-\mu_{12}|\sigma_{\gamma\gamma}}{\sigma_{\rm ann,2\gamma}}\right)^{1/2} \simeq 20\left(\frac{B}{10\,B_{\rm Q}}\right). \quad (9)$$

(The coefficient in the right expression is for $\hbar\omega \sim 1.25\,m_e c^2$, corresponding to $\beta \sim 0.6$ for the created pair.)

The annihilation of $e^{\pm}$ is distributed along the confining magnetic field. The net annihilation rate within a flux rope of cross section $\delta A_\perp$ will be obtained in the approximation of pressure equilibrium along $\boldsymbol{B}$. Given that $\delta A_\perp = (B/B_{\rm NS})^{-1}\delta A_{\perp,\rm NS}$ (here "NS" denotes the value where the rope connects to the star), the density profile is

$$n_p = n_{p,\rm NS}\frac{\delta A_{\rm NS}}{\delta A} = n_{p,\rm NS}\frac{B}{B_{\rm NS}}. \quad (10)$$

Consider first the part of a flux rope where $B > B_{\rm Q}$. From Equation (8), the annihilation rate integrated across the cross section of the rope is distributed uniformly with respect to the longitudinal coordinate $\ell_\parallel = \int \boldsymbol{dx}\cdot\hat{B}$,

$$\frac{d(\delta\dot{N}_{\rm ann,2\gamma})}{d\ell_\parallel} = \delta A_\perp\, n_p^2\, \sigma_{\rm ann,2\gamma}(\beta, B)\,\beta c = \delta A_{\perp,\rm NS}\, n_{p,\rm NS}^2\, \sigma_{\rm ann,2\gamma}(\beta, B_{\rm NS})\,\beta c. \quad (11)$$

This quantity is integrated along each flux tube from its intersection with the star to at most a polar angle $\theta = \pi/2$.

Farther away from the surface of the star, where the magnetic field is weaker, the annihilation cross section can instead be approximated by the vacuum expression (V. B. Berestetskii et al. 1982):

$$\sigma_{\rm ann,2\gamma}[B=0] = \frac{\pi r_e^2(1-\beta^2)}{4\beta}\left[\frac{3-\beta^4}{\beta}\ln\left(\frac{1+\beta}{1-\beta}\right) - 2(2-\beta^2)\right], \quad (12)$$

here defined in the COM frame. We take the annihilation cross section $\sigma_{\rm ann,2\gamma}$ to be the minimum of Equations (8) and (12).

One sees that most annihilations are concentrated in the zone $B > B_{\rm Q}$ on flux ropes extending far enough that the magnetic field drops below $B_{\rm Q}$.

2.3.2. Surface Annihilation

Positrons also annihilate at the surface of the star. Above the surface, an atmosphere of ions and electrons backscatters incident charged particles, reducing surface annihilation. The restriction of charged particle motion to one dimension (along $\boldsymbol{B}$) leads to significant flux of reflected pairs: only one-third of those incident on the atmosphere are absorbed. Warm positrons and electrons both backscatter off ions with a cross section $\sigma_{i\pm} = \pi r_e^2/\beta^4\gamma^4$ (G. G. Pavlov & D. G. Yakovlev 1976; A. Kostenko & C. Thompson 2019), but positrons backscatter more rapidly off atmospheric electrons through the one-photon annihilation channel. The Coulomb cross section $\sigma_{i\pm}$ is smaller than $\sigma_{\rm ann,1\gamma}/2$ by a factor $\sim 0.06\,(B/10\,B_{\rm Q})$ (for a typical particle speed $\beta \sim 0.6$: see Equation (1)).

Annihilation takes place at greater depths than backscattering, but still at a moderate depth to O-mode electron scattering. To see this, we note that annihilation into two photons (both below threshold for pair conversion) has a cross section $\sigma_{\rm ann,2\gamma} \ll \sigma_{\rm ann,1\gamma}$. An absorbed positron reaching an electron column N_e below the surface has traversed a total column $N_e^2 \cdot \sigma_{\rm ann,1\gamma}/2$; it annihilates at a mean depth

$$\tau_O < \tau_{\rm T} \sim \frac{\sigma_{\rm T}}{(\sigma_{\rm ann,2\gamma}\sigma_{\rm ann,1\gamma}/2)^{1/2}} = 0.3\left(\frac{B}{10\,B_{\rm Q}}\right). \quad (\beta \sim 0.6) \quad (13)$$

The backscattered particle fraction is derived straightforwardly. Given that scattering occurs on average at a column N_s of target particles, the probability of first scattering at column N_1 is $dP_1 = e^{-N_1/N_s}\,dN_1/N_s$, and the total probability to escape the atmosphere after this first scattering is $P_{1,esc} = \int_0^\infty (dN_1/N_s)e^{-2N_1/N_s} = 1/2$. The probability to escape after $2n$ more backscatterings is a factor 4^{-n} times smaller, leading to a total backscattering probability

$$P_{\rm esc} = \sum_{n=0}^{\infty} P_{2n+1,esc} = \frac{2}{3}. \quad (14)$$

Note that this result does not depend on the tilt of the magnetic field with respect to gravity.

The scattering of positrons back into the magnetosphere is primarily by warm electrons. Note that collisions of warm and cold electrons do not change the one-dimensional electron distribution function, meaning that a population of warm electrons will be present in the outer atmosphere. Warm electrons can backscatter off ions before cooling by bremsstrahlung emission, and so upward-moving warm electrons will have comparable density to downward moving warm electrons in the shallow layer where positrons experience one-photon annihilation.

We must check that a positron does not first cool and annihilate in the atmosphere before backscattering. A positron can exchange energy and momentum with a cool atmospheric electron, given that the scattering is restricted to one spatial dimension. The resulting cool positron may either get reheated by a collision with a warm electron or instead annihilate (most likely with a cool atmospheric electron). Given a density $n_{e,c} \sim N_e/h$ of cool electrons in an atmosphere of scale height $h \sim k_B T_{e,c}/m_p g$ and mean thermal speed $\beta_c \sim (k_B T_{e,c}/m_e c^2)^{1/2}$, we may compare the rates of (i) annihilation into two photons (both below the threshold for single-photon pair creation) and (ii) backscattering off warm electrons with speed $\beta_h \sim 0.6$ and mean density $n_{e,h} = n_{p,NS} \simeq \tau_{T,mag}/\sigma_T R_{NS}$. At a column $N_e \sim [\sigma_{ann,1\gamma}(\beta_h)/2]^{-1}$ typical of backscattering, we find

$$\frac{\beta_c\, n_{e,c}\, \sigma_{\gamma 2,ann}(\beta_c)}{\beta_h\, n_{e,h}\, \sigma_{ann,1\gamma}(\beta_h)/2} \sim \frac{\alpha_{em}^2}{\tau_{T,mag}}\left(\frac{B}{B_Q}\right)\frac{m_p g R_{NS}}{m_e c^2} = 0.013\, \tau_{T,mag}^{-1}\left(\frac{B}{B_Q}\right). \quad (15)$$

Note that $T_{e,c}$ and β_c cancel from this expression. Atmospheric annihilation of positrons is therefore a second-order effect in our MC models, where $\tau_{T,mag} \sim 0.3$ and $B = (4-10)B_Q$.

The net result is that, counting only downward-moving positrons, we have a net surface annihilation rate at each end of a flux rope,

$$\delta\dot{N}_s = \delta A_{\perp,NS} \cdot \frac{1}{3} \cdot \frac{1}{2} n_{p,NS}\beta c = \frac{1}{9} R_{NS}^2\, \delta\sqrt{3\cos^2\theta + 1}\; \delta\phi \cdot n_{p,NS}\beta c; \quad (16)$$

here, δX represents the change in angular quantity X across the flux bundle.

2.3.3. Radiation-pressure-driven Outflow near the Poles

There is enhanced loss of plasma from the inner magnetosphere on field lines reaching far enough from the star for $e^{\pm}$ to resonantly scatter kiloelectronvolt blackbody photons. Taking the photon and scattering particle to move radially near the magnetic poles, the resonant radius corresponding to $\omega = \omega_{ce} = eB(r)/m_e c$ in the particle rest frame is

$$\frac{r_{res}}{R_{NS}} = \left[\gamma(1+\beta)\frac{eB_{pole}}{m_e c\omega}\right]^{1/3} = 30\, \frac{B_{pole,15}^{1/3}}{(\hbar\omega/\,\mathrm{keV})^{1/3}} \qquad (\beta = 0.6). \quad (17)$$

Dipolar field lines reaching this radius are anchored closer than an angle $\theta_{res} \simeq (r_{res}/R_{NS})^{-1/2} \sim 10^\circ$ to the poles (with surface magnetic flux density B_{pole}). Pairs moving along this polar flux bundle feel a very strong drag when moving differentially with respect to the photon field. Because the pair kinetic energy flux below the resonance radius is much smaller than the X-ray Poynting flux, the pairs are forced rapidly outward in this zone. The corresponding particle loss is

$$\delta\dot{N}_{res} = \frac{1}{3} R_{NS}^2\, \delta\sqrt{3\cos^2\theta + 1}\; \delta\phi \cdot n_{p,NS}\beta c \quad (\theta < \theta_{res}). \quad (18)$$

The strength of this coupling may be gauged as follows. The radial force imparted to the pairs by a spherical flow of X-rays with luminosity L_X is $f_{rad} = \gamma(1-\beta)(2\pi^2 e^2/4\pi r_{res}^2 m_e c^2) dL_X/d\omega$. Maintaining a radial pair velocity $\beta < 1$ within this photon field would require a large net energy input to the pairs:

$$\frac{f_{rad} \cdot (1-\beta) r_{res}}{m_e c^2} \sim 250\, \frac{(dL_X/d\ln\omega)_{35}}{B_{pole,15}^{1/3}(\hbar\omega/\mathrm{keV})^{2/3}}, \quad (19)$$

evaluated here for $\beta \sim 0.6$.

2.3.4. Balance between Pair Creation and Annihilation

We may finally determine the equilibrium number of pairs on a given magnetic flux bundle from the solution to the following quadratic equation for $n_{p,NS}$, obtained by summing the loss terms from Equations (11), (16), and (18).

$$\delta\dot{N}_p = 0 = \delta\dot{N}_{\gamma+\gamma\to e^+ + e^-} - \delta\dot{N}_{ann,2\gamma} - \delta\dot{N}_s - \delta\dot{N}_{res}. \quad (20)$$

3. Magnetic Field and Currents

The changing X-ray pulse profiles of magnetars suggest the presence of nondipolar structure in the electric currents whose dissipation drives nonthermal X-ray emission (e.g., P. M. Woods et al. 2001). The geometry of the underlying magnetic field is only weakly constrained. For our purposes, the two essential components are (i) a global dipole magnetic field, part of which connects to the outer magnetosphere and (ii) localized currents connecting to crustal shear bands. These localized currents are closely aligned with the field but generally do not flow near the magnetic poles; they involve localized shearing of the field.

Simple choices of the magnetic field and currents will suffice to demonstrate the effects of nonlocal $\gamma - \gamma$ pair creation. The large-scale field may be weakly twisted but is assumed to be predominantly dipolar. The magnetic and particle density fields are represented in flat spacetime. Outside the star (radius R_{NS}) and in spherical coordinates (r, θ, ϕ),

$$\boldsymbol{B}(r,\theta) = \nabla\Psi \times \nabla\phi = \frac{1}{r\sin\theta}\nabla\Psi \times \hat{\phi}. \quad (r \geqslant R_{NS}). \quad (21)$$

Poloidal magnetic flux surfaces are isocontours of the function

$$\Psi(r,\theta) = \sin^2\theta\, \frac{\mu}{r} = \frac{\mu}{\mathcal{R}}. \quad (22)$$

Here, μ is the magnetic moment of the star, and $\mathcal{R} = r/\sin^2\theta = R_{NS}/\sin^2\theta_\star$ is the largest radius reached by a dipolar field line that is anchored at polar angle $\theta_\star$.

We explore four different configurations in which the currents are confined to discrete arcade structures (Table 1 and Figure 2). Electron–positron plasma, supporting the current and emitting a hard spectrum of X-rays and gamma-rays, is present in these twist zones. Because charged particles can flow along the magnetic field, but are confined by radiative de-excitation to the lowest Landau state, these emission structures are defined by poloidal slices covering a discrete range of $\mathcal{R}$. They also cover a discrete range of azimuthal angle ϕ. In the case of the quarter shell structure (model 1), a mirror-symmetric arcade oppositely placed is also considered (model 2). Adding this second emission component widens the exposure to gamma-rays and induces stronger angular dispersion in overlapping rays.

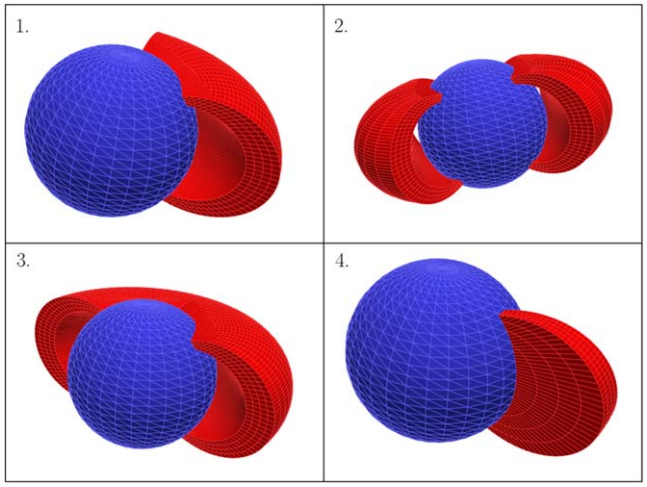

Figure 2. Hard X-rays and gamma-rays are emitted from the surfaces of $e^{\pm}$-loaded magnetic arcades (red) that are anchored to shear bands in the magnetar crust. MC calculations of photon emission and collisions are carried out for the four cases shown. Top left: quarter shell extending over $\Delta\phi = \pi/2$. Top right: two antipodal quarter shells. Bottom left: half shell extending over $\Delta\phi = \pi$. Bottom right: thin wedge extending over $\Delta\phi = \pi/16$. Parameters are listed in Table 1.

Table 1
Parameters of Gamma-Ray Emission Structures

Case	$\theta_{\star,1}$	$\Delta\theta_\star$	$\Delta\phi$
Quarter Shell	$\pi/4$	0.1234	$\pi/2$
Half Shell	$\pi/4$	0.1234	π
Thin Wedge	$\pi/4$	$\pi/4$	$\pi/16$

Note. $\theta_{\star,1}$ is the angle closest to the pole where the emission surface intersects the star, $\Delta\theta_\star$ is the range of polar angle covered by the emission structure, and $\Delta\phi$ is the range in azimuthal angle. One case (2 in Figure 2) includes a second quarter shell structure that is offset by angle π in azimuth from the first.

3.1. Polar Magnetic Shear

Magnetars experiencing accelerated spindown appear to have inflated magnetospheres[4] supporting a polar twist (C. Thompson et al. 2002; C. Thompson 2008b; A. M. Beloborodov 2009). One of our principal goals is to compare the density of pairs created nonlocally by $\gamma - \gamma$ collisions with the minimal (critical) density that sustains a polar twist. When the global current can be supplied in this way, the polar voltage is greatly reduced.

A fixed azimuthal offset $\Delta\phi_{\rm N-S}$ between the two magnetic hemispheres will generate a current

$$\frac{4\pi}{c}\boldsymbol{J} = \nabla \times \boldsymbol{B} \simeq \Delta\phi_{\rm N-S}\frac{\boldsymbol{B}}{\mathcal{R}}. \tag{23}$$

The critical space density of pairs $n_p = n_{e^+} = n_{e^-}$ of charge $\pm e$ drifting with speed $\pm\beta c$ is $n_p = J/2|e|\beta c$. Hence,

$$n_{\rm crit} = \frac{\Delta\phi_{\rm N-S}}{8\pi\beta}\frac{B}{e\mathcal{R}}. \tag{24}$$

[4] Related possibilities are that the polar field lines support an enhanced persistent flux of Alfvén waves (C. Thompson & O. Blaes 1998) or relativistic particles (A. K. Harding et al. 1999). Some fine tuning is required to launch the Alfvén wave or particle flow on a sufficiently narrow field bundle that it strongly amplifies the spindown, even while the hard X-ray continuum has already diminished (R. F. Archibald et al. 2015).

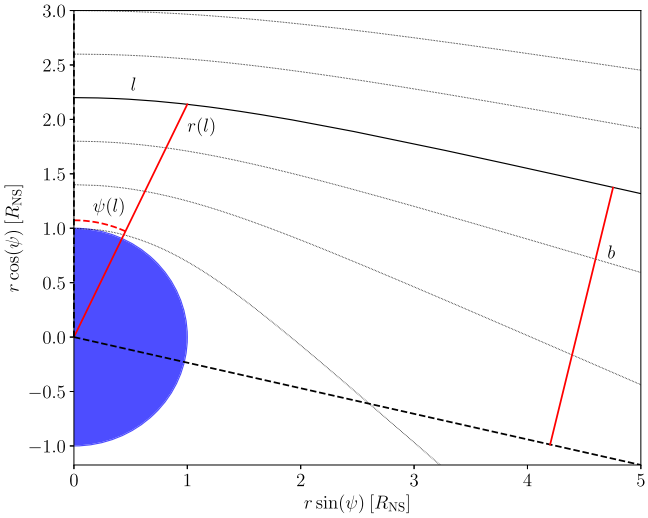

Figure 3. Sample planar photon trajectories (black curves) around a nonrotating magnetar of mass 1.4 $M_\odot$ and radius $R_{\rm NS} = 10$ km. Coordinates r and ψ in the plane of the geodesic are labeled by impact parameter b. The geodesic library includes cases with $r_{\rm min} < R_{\rm NS}$, which intersect the line $\Psi = 0$ with an angle smaller than $\pi/2$.

This density is usefully normalized by the Thomson cross section $\sigma_{\rm T}$ to give a characteristic optical depth that is not far off the optical depth to scattering for O-mode X-rays,

$$2n_{\rm crit}\sigma_{\rm T}R_{\rm NS} = \frac{2\Delta\phi_{\rm N-S}}{3\beta}\alpha_{\rm em}\left(\frac{B}{B_{\rm Q}}\right)\left(\frac{R_{\rm NS}}{\mathcal{R}}\right). \tag{25}$$

Plasma of this minimal density is generally optically thin to electron–positron annihilation and is too dilute to support the collisional state.

4. Photon Propagation

The curvature of photon trajectories is the principal general relativistic effect that must be taken into account to calculate the $e^{\pm}$ loading of the magnetic field outside the gamma-ray emitting zones. The refraction of O-mode trajectories due to a varying index of refraction is subdominant to gravitational lensing when the surface field is of the strength considered here ($4-10\,B_{\rm Q}$). Some sample photon trajectories around a nonrotating star are shown in Figure 3.

Lensing increases the volume that is exposed to pair-creating gamma-rays if the emitting plasma is localized on one side of the star. To illustrate the importance of this effect, Figure 4 shows the part of the stellar surface that is directly impacted by photons that are emitted in all directions from the surface of a slender magnetic fibril.

A photon trajectory outside a nonrotating star is a planar geodesic in Schwarzschild spacetime. This curve can be parameterized by coordinates (r, ψ) in a reference plane. Our MC method, detailed in Section 5, builds a geodesic library that can be mapped onto general emission coordinates and directions. The angle $\psi = 0$ is aligned with the closest approach (radius $r_{\rm min}$) on rays that do not intersect the star. Integrating from $\psi = 0$, a ray with impact parameter b is determined by (Figure 3; L. D. Landau & E. M. Lifshitz 1975)

$$\psi(r) = \int_{r_{\rm min}}^{r}\frac{d\psi}{dr}dr = \int_{r_{\rm min}}^{r}\frac{dr}{r^2}\left[\frac{1}{b^2} - \frac{1}{r^2}\left(1 - \frac{r_g}{r}\right)\right]^{-1/2}. \tag{26}$$

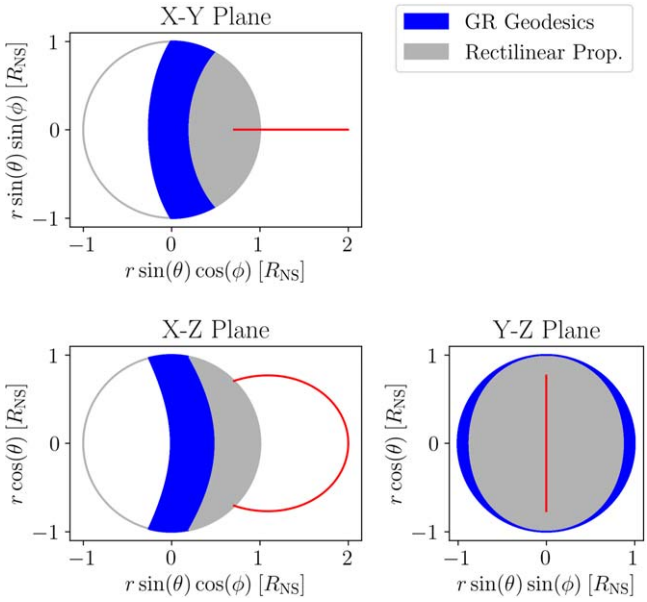

Figure 4. Photons emitted from a slender fibril in a dipolar magnetic field can propagate through much—but not all—of the inner magnetosphere. Some photons directly impact the surface. The irradiated part of the surface is plotted in gray under the assumption of rectilinear propagation. General relativistic geodesics are able to reach the expanded blue zone, thereby significantly increasing the irradiated portions of the stellar surface and surrounding magnetosphere. Here, the emitting fibril (red) is anchored at polar angle $\theta_\star = \pi/4$.

Here, $r_g = 2GM/c^2$ is the gravitational radius. The minimum radius is related to the impact parameter by:

$$r_{\rm min} = 2\sqrt{\frac{b^2}{3}}\cos\left[\frac{1}{3}\arccos\left(\frac{-3r_g}{2}\sqrt{\frac{3}{b^2}}\right)\right]. \tag{27}$$

The geodesic plane is defined in the frame of the star by a choice of emission point $\boldsymbol{r}_0$ and direction $\hat{k}_0$, as seen in Figure 5. The normal vector $\hat{n}$ and basis vectors are related by $\hat{r}_0$ and $\hat{\psi}_0$:

$$\hat{n} \equiv \frac{\hat{k}_0 \times \hat{r}_0}{|\hat{k}_0 \times \hat{r}_0|}; \quad \hat{\psi}_0 \equiv \hat{n} \times \hat{r}_0. \tag{28}$$

Gravitational redshifting of the photon energy is readily included and is also accounted for in our MC treatment. From an emission point at radius r_0 to a pair creation site (or surface impact) at radius $r_{\rm abs}$, a photon of initial energy ω_0 redshifts or blueshifts to

$$\omega = \left[\frac{g_{tt}(r_0)}{g_{tt}(r_{\rm abs})}\right]^{1/2}\omega_0 = \left[\frac{1 - r_g/r_0}{1 - r_g/r_{\rm abs}}\right]^{1/2}\omega_0. \tag{29}$$

The redshift is a 10% correction, which can be significant because the broad emission spectrum cuts off sharply above energy $\sim m_e c^2$ when the effects of multiple scattering and self-absorption in the emitting plasma are accounted for (see Equation (33) below and Figure 14 of C. Thompson & A. Kostenko 2020).

Our MC treatment does not account for the general relativistic volume effect or the corresponding distortion of the background magnetic field. Calculating the equilibrium pair abundances depends on summing the pair creation rate over each dipolar magnetic flux element. We choose a spatial grid aligned with the magnetic field, which is easy for a flat-space dipole, but very complicated for more general field configurations.

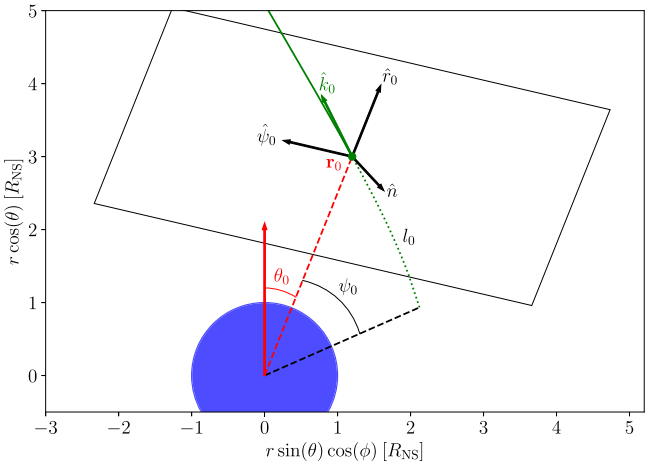

Figure 5. Orientation of a sample geodesic plane in the frame of the star. The normal to the plane is defined in terms of the emission point $\boldsymbol{r}_0 = (r_0, \theta_0, \phi_0)$ and initial direction $\hat{k}_0$ by $\hat{n} = \hat{k}_0 \times \boldsymbol{r}_0/|\hat{k}_0 \times \boldsymbol{r}_0|$. Variables in the geodesic plane are initial radius r_0 and ψ_0, the angle between the emission point and the closest approach.

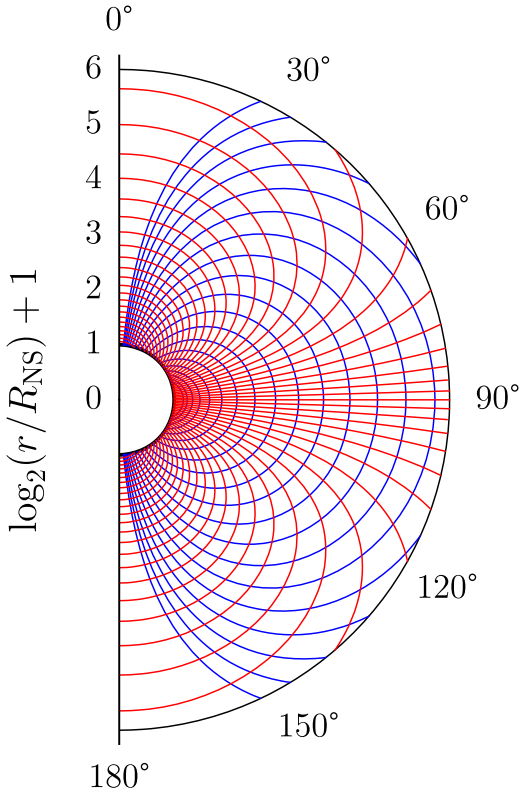

Figure 6. Spatial grid aligned with flat-space dipolar magnetic field. The field lines (blue) bounding spatial cells are curves of constant $\mathcal{R} = r/\sin^2\theta$. The complementary set of boundary lines (red) are curves of constant $\cos\Theta = [1 + \ln(r_{\rm pole}/r)]^{-1}$.

5. Monte Carlo Method

5.1. Spatial and Angular Grids

The magnetospheric grid is aligned with the dipolar magnetic field (Figure 6), with the expectation that the

Table 2
Grid and Emission Parameters

Parameter	Value
$R_{\rm NS}$	10 km
$M_{\rm NS}$	1.4 $M_\odot$
$R_{\rm max}$	32 $R_{\rm NS}$
$N_{\mathcal{R}}$	20
N_ϕ	64
N_θ	64
$N_{\theta k}$	8
$N_{\phi k,\rm max}$	8
N_ω	128
$\hbar\omega_{\rm min}$	15 keV
$\hbar\omega_{\rm max}$	2.5 $m_e c^2$
$\hbar\omega_0$	1.5 $m_e c^2$

gamma-ray emitting surfaces are magnetic flux surfaces. Grid cells are bounded by surfaces of constant $\mathcal{R}$ (poloidal magnetic flux), azimuthal angle ϕ, and a conjugate angular variable chosen as $\cos\Theta = [1 + \ln(r_{\rm pole}/r)]^{-1}$. The isocontours of Θ are approximately orthogonal to those of $\mathcal{R}$; they are labeled by the radius $r_{\rm pole}$ at which they intersect the polar axis ($\theta = 0$), or equivalently by the angle $\tilde{\theta}_\star$ at which they intersect the star. The number of grid cells in each of these three coordinates is $(N_{\mathcal{R}}, N_\Theta, N_\phi) = (20, 64, 64)$, including both magnetic hemispheres (Table 2).

The grid is uniformly spaced in ϕ, in $\ln(\mathcal{R}/R_{\rm NS})$, and in $\tilde{\theta}_\star^2$ over the range $0 < \tilde{\theta}_\star < \pi/2$. It is symmetric on reflection between the northern and southern magnetic hemispheres, filling a spherical zone between radii $r = R_{\rm NS}$ and $r = R_{\rm max} = 32R_{\rm NS}$. (Cells reaching $r = R_{\rm max}$ are cut off at that spherical radius.) Additional sets of cells cover the magnetic north and south polar axes; these are bounded by $\mathcal{R} > \mathcal{R}_{g,\rm max} = 174\,R_{\rm NS}$ and by the variable $r_{\rm pole}$ (or equivalently $\tilde{\theta}_\star$), but are not divided in ϕ.

The volume of a cell bounded by $(\mathcal{R}_1, \mathcal{R}_2)$, $(r_{\rm pole,1}, r_{\rm pole,2})$, and (ϕ_1, ϕ_2) is given by

$$V = (\phi_2 - \phi_1)\int_{\mathcal{R}_1}^{\mathcal{R}_2}\mathcal{R}^2\int_{\theta_1(\mathcal{R})}^{\theta_2(\mathcal{R})}\sin^7\theta d\theta d\mathcal{R} \tag{30}$$

where $\theta_i(\mathcal{R})$ is the polar angle at which the Θ isocontour labeled by $r_{{\rm pole},i}$ intersects the flux surface labeled by $\mathcal{R}$. This is given implicitly by

$$\frac{r_{{\rm pole},i}}{\mathcal{R}} = (1 - x_i^2)e^{(1-x_i)/x_i}; \qquad \cos\theta_i \equiv x_i, \tag{31}$$

excepting when the intersection is implied to sit outside the computational domain (outer radius $R_{\rm max}$).

The orientation of rays passing through each spatial cell is represented by an additional angular grid. We choose spherical angular coordinates (θ_k, ϕ_k), with $\theta_k = 0$ aligned with $\theta = 0$ in each spatial cell. The angular bins are uniformly divided in θ_k, with $N_{\theta k} = 8$ rows. The number of ϕ_k-cells dividing each row of average polar angle $\bar{\theta}_k$ is given by $N_{\phi k} = \lceil N_{\phi k,\rm max}\sin(\bar{\theta}_k)\rceil$, with $N_{\phi k,\rm max} = 8$.

5.2. Geodesic Library

Instead of solving the geodesic equation for each of billions of sample photons, we build a reference library of planar Schwarzschild geodesics, following the method described in Section 4. These trajectories are labeled by impact parameter b and uniformly distributed in $\log b$; we also include the radial trajectory ($b = 0$). They are mapped directly into flat space and parameterized by the path length l. (Once again, our main goal in calculating geodesics is to account for blind spots in the photon density field produced by a localized emission structure; the general relativistic corrections to path length and photon residency time are $O(r_g/r) \sim 10\%$.)

Given a randomly chosen emission position $\boldsymbol{r}_0$ and ray tangent vector $\hat{k}_0$, we obtain the planar basis $(\hat{n}, \hat{\psi}_0)$ from Equation (28). From the emission radius r_0 and emission angle $\theta_{kr} = \cos^{-1}(\hat{k}_0 \cdot \hat{r})$, we compute the impact parameter $b = r_0\sin\theta_{kr}(1 - r_g/r_0)^{-1/2}$ of the trajectory and then linearly interpolate between the two geodesics with the nearest b values in the library. We then find the initial path length l_0, implicitly defined as $r(l_0) = r_0$, and angle $\psi_0 = \psi(l_0)$. The trajectory $\boldsymbol{r}$ and ray tangent vector $\hat{k}$ are easily computed as a function of the length l of the embedded geodesic:

$$\hat{r} = \frac{\boldsymbol{r}}{r} = \cos[\psi(l) - \psi_0]\hat{r}_0 + \sin[\psi(l) - \psi_0]\hat{\psi}_0;$$
$$\hat{\psi} = \hat{n} \times \hat{r}; \quad \hat{k} = \frac{dr}{dl}\hat{r} + r\frac{d\psi}{dl}\hat{\psi}. \tag{32}$$

The endpoint of the trajectory corresponds to $r = R_{\rm max}$ or $r = R_{\rm NS}$, depending on whether it escapes the grid or first hits the star.

5.3. Photon Emission and Residency

The photon flux is assumed to be uniform across the surface of each emission structure and locally isotropic in direction. The emission points of trial photons are therefore chosen randomly, with a uniform distribution by area. The initial $\hat{k}_0$ is defined relative to the plane tangent to the emitting surface, being decomposed as $\hat{k}_0 = \cos\alpha\,\hat{S} + \sin\alpha\cos\beta\,\hat{B} + \sin\alpha\sin\beta\,\hat{S}\times\hat{B}$, where $\hat{S}$ is the normal to the emitting surface. Isotropic emission corresponds to probability uniform in the direction cosine $\cos\alpha = \hat{k}_0 \cdot \hat{S}$ and uniform in β. We only consider outward emission with $\cos\alpha > 0$.

The source spectrum is chosen to represent annihilation bremsstrahlung emission from a collisional plasma, as modified by the effects of reabsorption and multiple electron scattering. Following the QED MC results of C. Thompson & A. Kostenko (2020), we choose

$$\frac{dL_\gamma}{d\omega} = c(n)\frac{L_0}{\omega_0}e^{-(\omega/\omega_0)^n}, \tag{33}$$

where $c(n)$ is a normalization constant, and L_0 is the total luminosity. The photon number spectrum $\hbar^{-1}dL_\gamma/d\omega$ is flat close to the energy $\hbar\omega_0$, above which it cuts off hyper-exponentially. The parameters $n = 4$, $\hbar\omega_0 = 1.5\,m_e c^2$ fit the QED MC spectra that correspond to a scattering depth $\sim 2-10$ across the source plasma. The energies of trial photons are drawn from the range $\{\hbar\omega_{\rm min} = 15\ {\rm keV}, \hbar\omega_{\rm max} = 2.5\,m_e c^2\}$, with $N_\omega = 128$ frequency bins spaced uniformly in $\log(\omega)$. Photons that exceed the local pair conversion threshold energy $2m_e c^2/\sin\theta_{kB}$, either at emission or at some point on their trajectory, are assumed to be absorbed.

Each photon trajectory intersects a certain number of grid cells. The change in path length across a given cell, $l_i \to l_f$, is determined by bisection. A characteristic photon direction within the cell is $\hat{k} = [\hat{k}(l_f) + \hat{k}(l_i)]/2$. The photon also experiences gravitational redshift according to Equation (29).

The residency time in a cell is $t = (l_f - l_i)/c$; this is summed separately for each bin, as defined by ω, $\hat{k}$ and cell number, to give a total residency time $t_{\rm tot}$.

After this procedure is completed for each photon (up to when it hits the star or escapes the grid), the photon number density distribution $n_\gamma(\hat{k}, \omega)$ is readily obtained. From the total photon emission rate

$$\Gamma_\gamma = \int \frac{1}{\hbar\omega}\frac{dL_\gamma}{d\omega}d\omega, \tag{34}$$

one has

$$n_\gamma \delta V = \frac{t_{\rm tot}\Gamma_\gamma}{N_\gamma}. \tag{35}$$

Here, δV is the cell volume, and N_γ is the total number of trial photons.

5.4. Photon Collision Rate

The total pair production rate is determined in each grid cell by discretizing the integral in Equation (3) into a sum,

$$\dot{N}_{\gamma\gamma\to e^+e^-} = \delta V \sum_{\hat{k}_1,\hat{k}_2}\sum_{\omega_1,\omega_2} n_1(\hat{k}_1, \omega_1) n_2(\hat{k}_2, \omega_2) \times |1 - \mu_{12}| c\, \sigma(\omega_1, \omega_2, \hat{k}_1, \hat{k}_2, B). \tag{36}$$

We then sum the pair production along each flux bundle. In the approximation that plasma drift is fast enough to equilibrate the pressure, according to Equation (10), the creation of pairs is balanced against loss due to outflow, surface collision, and annihilation using Equation (20). This gives the equilibrium surface density $n_{p,\rm NS}$ and the magnetospheric density following Equation (10).

To ensure that photon collisions are not overcounted, we sort and bin the summed pair creation rate by the energy carried by the more energetic photon. Gamma-rays with energies exceeding $2m_ec^2$ see a relatively large absorption optical depth, as pair conversion with photons of energy $\ll m_ec^2$ is kinematically allowed (Equation (5)) and has a higher cross section (Equation (6)). We apply a conservative cut on $\dot{N}_{\gamma\gamma\to e^+e^-}$ by removing collisions in photon energy bins where the implied absorption rate (of the more energetic photon) is larger than its production rate. Examples are shown in the Appendix. The net effect is that pair creation is dominated by collisions in which the higher photon energy lies in the range $(1-2)m_ec^2$. Photons of this energy also experience only limited electron scattering (Section 6.1): they are outside the resonance that enhances electron scattering at photon energies just below threshold for single-photon pair conversion ($\omega \lesssim \omega_{1\gamma}$; A. Kostenko & C. Thompson 2018).

This bound on pair creation rate is slightly relaxed for arcade model 4 (the thin slice geometry). Here we find that about one-half of the pair creation is concentrated in the cells adjacent to the emitting surface and, furthermore, that this photon absorption is mainly balanced by re-emission through volumetric $e^\pm$ annihilation. The net effect is to displace outward slightly the emission surface without changing its overall geometry. In model 4, we therefore allow the photon absorption rate to be up to 1.5 times the emission rate; in practice, this only affects the highest energy bin for which photon collisions are counted.

6. Results

Localized currents dissipating at a higher rate than their surroundings can be a copious source of low-energy gamma-rays near a magnetar. We present two sets of MC runs, both with luminosity $L_0 = 1 \times 10^{35}$ erg s^{-1}, and with (i) polar magnetic field $B_{\rm pole} = 10\,B_{\rm Q}$ and (ii) $B_{\rm pole} = 4\,B_{\rm Q}$, each involving 1.1×10^9 trial photons in each of the four sample emission structures. Figure 7 shows the photon density field surrounding a quarter shell arcade (model 1 in Figure 2).

This radiative output, which is dominated by gamma-rays of energy $\sim$0.5−1 MeV, is modest by the standards of quiescent magnetars. When the hard X-ray photon index is $\Gamma_X = -1$ (as adopted here), the output in the 15−60 keV band is only $10^{34}\,L_{0,35}$ erg s^{-1}; this drops to $\sim 0.5 \times 10^{34}\,L_{0,35}$ erg s^{-1} when Γ_X rises to −0.6, as measured in 1E 2259+586 and as inferred for pair annihilation in magnetic fields around $B_{\rm Q}$ (C. Thompson & A. Kostenko 2020).

The main results can be summarized as follows.

1. The pairs in equilibrium are more numerous than gamma-rays in the inner magnetosphere, as seen in Figure 8. In part, this is because photon collisions have a higher cross section than pair annihilation, $\sigma_{\gamma\gamma}/\sigma_{\rm ann,2\gamma} \sim (B/B_{\rm Q})^2$, and in part because there is significant reflection of downward moving pairs from the magnetar surface (Equation (14)).
2. The pairs created above the magnetic poles can easily supply the current associated with a weaker global magnetic twist, significantly limiting the polar voltage.
3. A moderate fraction of the emitted gamma-ray power is directly and indirectly absorbed by the magnetar, creating an inhomogeneous surface radiation profile. The large-scale magnetic field indirectly channels gamma-ray energy toward the magnetar in the form of a cloud of transrelativistic pairs, which dominate surface heating in comparison with the direct impact of gamma-rays.
4. A large optical depth to electron cyclotron scattering is produced around the resonance radius $r_{\rm res} \sim 20\,(B/10\,B_{\rm Q})^{1/3}\,R_{\rm NS}$ by the outward pressure of kiloelectronvolt photons on the pairs flowing near the magnetic poles. Rescattering in this zone will have a major impact on X-ray pulse profiles and X-ray polarization, but less so on the X-ray spectrum given the small net kinetic energy of the pairs.

6.1. Magnetospheric Pair Density Distribution

We first show results for the models with polar magnetic field $10\,B_{\rm Q}$ and higher cross section for conversion of gamma-rays to pairs. The case $B_{\rm pole} = 4\,B_{\rm Q}$ is treated separately in Section 6.5.

Table 3 lists the rates at which gamma-ray energy is converted to pairs (column (b)), absorbed by the magnetar surface (columns (c) and (e)), and converted back to photons by volumetric annihilation (column (d)). The pairs impacting the surface are assumed to move at speed $\beta = 0.6$, which is chosen to be larger than the mean $\beta = 0.4$ of the pairs created by $\gamma - \gamma$ collisions (as inferred from the MC simulation) to account for the additional energy gain from the gravitational potential. As a result, the sum of columns (c) and (d) is slightly larger than (b). The surface luminosity sums one-third the pair energy flowing through the stellar surface (see Section 2.3.2) and one-half the radiation energy flux incident directly on the surface; the latter factor accounts approximately for the effects of oblique

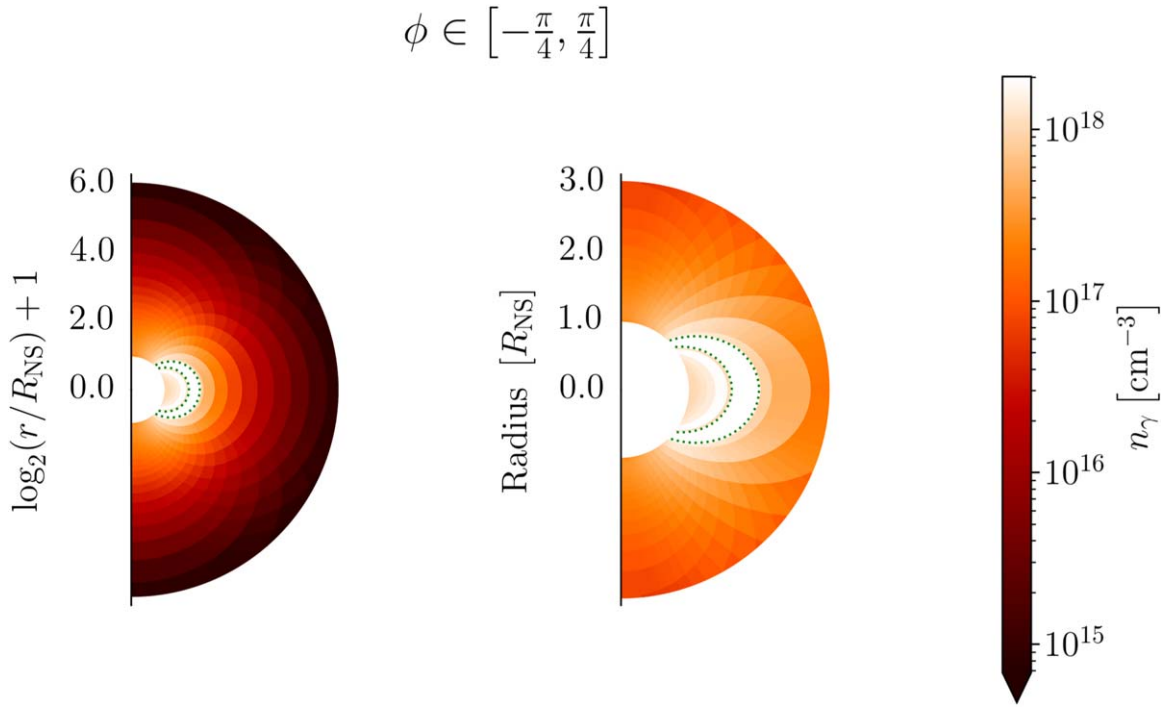

Figure 7. Photon density n_γ obtained by MC sampling of uniform and isotropic emission from the surface of the quarter shell arcade (depicted in white, extending to twice the radius of the star). Gamma-ray luminosity $L_0 = 10^{35}$ erg s^{-1}, with spectral parameters $\hbar\omega_0 = 1.5\, m_e c^2$ and $n = 4$ in Equation (33). The plotted value of n_γ is averaged over ϕ in the same quadrant from which gamma-rays are emitted. Left panel: full MC domain (log radius). Right panel: zoomed in to $r < 3R_{\rm NS}$ (linear radius).

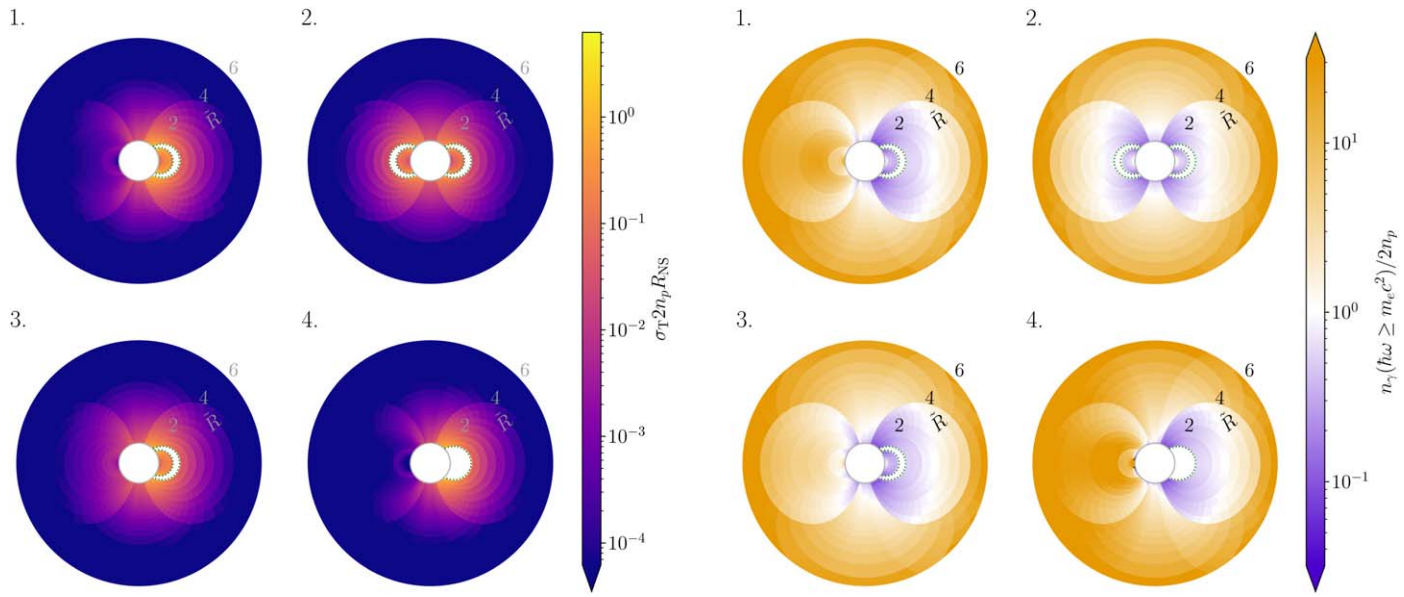

Figure 8. Left panel: poloidal slice of the equilibrium density $n_{e^+} + n_{e^-}$, normalized by $(\sigma_{\rm T} R_{\rm NS})^{-1}$, for all four types of emission structure (marked in white) and for $B_{\rm pole} = 10\, B_{\rm Q}$, $L_0 = 10^{35}$ erg s^{-1}. Right panel: ratio of density of pair-creating photons to pair density. Values plotted are an average over ϕ in the same quadrant from which gamma-rays are emitted. Pair creation via $\gamma + \gamma \rightarrow e^+ + e^-$ is integrated over the entire volume of a magnetic flux tube and balanced with volumetric annihilation, loss through the surface, and loss across the kiloelectronvolt electron cyclotron resonance surface (on field lines extending beyond $20(B/10\, B_{\rm Q})^{1/3}$ stellar radii). Radial density distribution along a flux tube is given by Equation (10). The radial variable is $\bar{R} \equiv \log_2(r/R_{\rm NS}) + 1$.

incidence and reflection. The effective temperature is computed from this absorbed energy flux.

A polar view of the near-surface particle density distribution is shown in Figure 9. Note that the pair density above the magnetar surface decreases as $\sim r^{-3}$. The following features will also be noted:

1. When the emission structure covers less than a quadrant in azimuth, pair creation is reduced in the antipodal zone. This effect is strongest for the thin poloidal wedge emission structure (model 4). In this case, the emission is too collimated for gravitational lensing to fill in the flux on the opposite side of the star, leaving a strongly pair-depleted shadow. However,

Table 3

Quantities Listed, for Each Emission Model (a): Efficiency of Conversion of Gamma-Ray Energy to Pairs (b), Fraction of Energy Lost to Annihilation at the Surface (c), Fraction Returned to Gamma-Rays through Volumetric Annihilation (d), Total Luminosity Absorbed at the Surface through Annihilation and Photon Impact (e), Peak Surface Effective Temperature (f), and the Area A_e Containing Half the Absorbed Surface Luminosity (g)

Model ($B_{\rm pole} = 10\,B_{\rm Q}$; $L_{0,35} = 1$)	γ Conv.	Surf. Ann.	Vol. Ann.	Surf. Lum. [erg s^{-1}]	Max Temp [K]	$A_e/A_{\rm NS}$
(a)	(b)	(c)	(d)	(e)	(f)	(g)
1. Quarter Shell	12%	9.9%	2.9%	1.1×10^{34}	2.8×10^{6}	7.1%
2. Double Quarter	8.9%	8.4%	1.0%	9.7×10^{33}	2.3×10^{6}	15%
3. Half Shell	11%	9.6%	1.9%	1.0×10^{34}	2.5×10^{6}	12%
4. Thin Wedge	19%	12%	8.2%	1.2×10^{34}	3.7×10^{6}	2.6%
5. Thin Wedge*	11%	8.3%	3.0%	8.0×10^{33}	3.1×10^{6}	3.7%
Model ($B_{\rm pole} = 4\,B_{\rm Q}$; $L_{0,35} = 1$)	γ Conv.	Surf. Ann.	Vol. Ann.	Surf. Lum. [erg s^{-1}]	Max Temp [K]	$A_e/A_{\rm NS}$
(a)	(b)	(c)	(d)	(e)	(f)	(g)
1. Quarter Shell	5.2%	4.7%	0.7%	7.5×10^{33}	2.5×10^{6}	7.7%
2. Double Quarter	3.9%	3.8%	0.2%	7.0×10^{33}	2.1×10^{6}	16%
3. Half Shell	4.8%	4.5%	0.4%	7.4×10^{33}	2.2×10^{6}	13%
4. Thin Wedge	9.2%	6.8%	2.8%	8.9×10^{33}	3.3×10^{6}	3.0%
5. Thin Wedge*	5.4%	4.7%	1.0%	5.9×10^{33}	2.8×10^{6}	3.9%

Note. The top and bottom sections of the Table show results for (i) polar magnetic field 10 $B_{\rm Q}$ and luminosity $L_0 = 1 \times 10^{35}$ erg s^{-1} and (ii) magnetic field 4 $B_{\rm Q}$ and luminosity $L_0 = 1 \times 10^{35}$ erg s^{-1}. Annihilation energy in (c) includes change in gravitational energy ($\beta \to 0.6$ at surface). The Thin Wedge* shows results after excising one layer of grid cells adjacent to the emission surface.

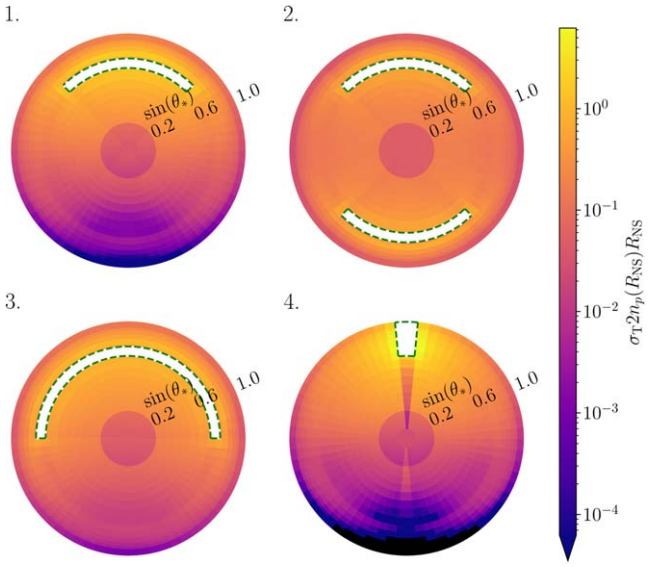

Figure 9. Equilibrium density $n_{e^+} + n_{e^-}$ at the surface of the star, normalized by $(\sigma_{\rm T} R_{\rm NS})^{-1}$, for all four types of emission structure (marked in white) and for $B_{\rm pole} = 10\,B_{\rm Q}$, $L_0 = 10^{35}$ erg s^{-1}. View is along along a polar magnetic axis, with radial coordinate $\sin\theta_\star$ and azimuthal coordinate ϕ.

some enhancement due to lensing is seen directly antipodal to the emitting wedge.

2. The plasma density is lower near the poles, on field lines extending out to the kiloelectronvolt resonant scattering radius $r_{\rm res}$ (Equation (17)), where they are pushed outward.

3. A dissipation rate $L_0 = 10^{35}$ erg s^{-1} is an approximate upper bound for optically thin radiation transport through a magnetic field with polar strength $10\,B_{\rm Q}$. Most gamma-ray collisions are concentrated close to the emission surface around the two most localized structures (the quarter shell, model 1, and thin poloidal wedge, model 4). This has the effect of pushing the emission surface outward from the edge of the twist zone where ohmic dissipation is concentrated. In model 4, one half of the annihilations occur in the set of grid cells immediately adjacent to the wedge (see Table 1). Note also that the characteristic O-mode X-ray scattering depth above the stellar surface is reduced by a factor 0.1−0.2 compared with the quantity $\sigma_{\rm T} 2 n_{p,{\rm NS}} R_{\rm NS}$ plotted in Figure 9 after taking into account that n_p varies over a length scale $\sim R_{\rm NS}/3$, the effect of ray orientation on scattering ($\sigma_{\rm O} \simeq \sin^2\theta_{kB}\sigma_{\rm T}$), and the reduction in density above the magnetar surface, $n_p(r) \propto r^{-3}$.

6.2. Supporting a Weaker Global Current

Figure 10 compares the pair density produced nonlocally by $\gamma - \gamma$ collisions with the minimum needed to support a global twist (Equation (24)). In all four arcade models, this threshold is easily reached near the poles—even when the global twist is strong enough ($\Delta\phi_{\rm N-S} \sim 1$ radian) to induce an order-of-magnitude increase in spindown torque (C. Thompson et al. 2002). The pair density falls below threshold only in some gamma-ray shadows that are antipodal to an emitting arcade.

6.3. Surface Heating

Figure 11 shows a polar view of the surface energy flux produced by pair annihilation (right panel) and photon impact (left panel). The annihilation energy flux is $(1/3) \cdot (1/2) \cdot 2 n_{p,{\rm NS}}\,\gamma\beta m_e c^3$, accounting for the proportions of pairs that are absorbed rather than reflected and are moving downward to the star. Direct photon impact makes a generally smaller contribution to surface heating.

This surface flux is inhomogeneous and will contribute to lower-energy X-ray pulsations. Note also that heating from positron annihilation is more evenly distributed across the stellar surface, as the magnetic field can collect pairs farther out in the magnetosphere and channel them toward the surface.

The corresponding effective temperature is shown in the left panel of Figure 12, and the relative proportions of the two

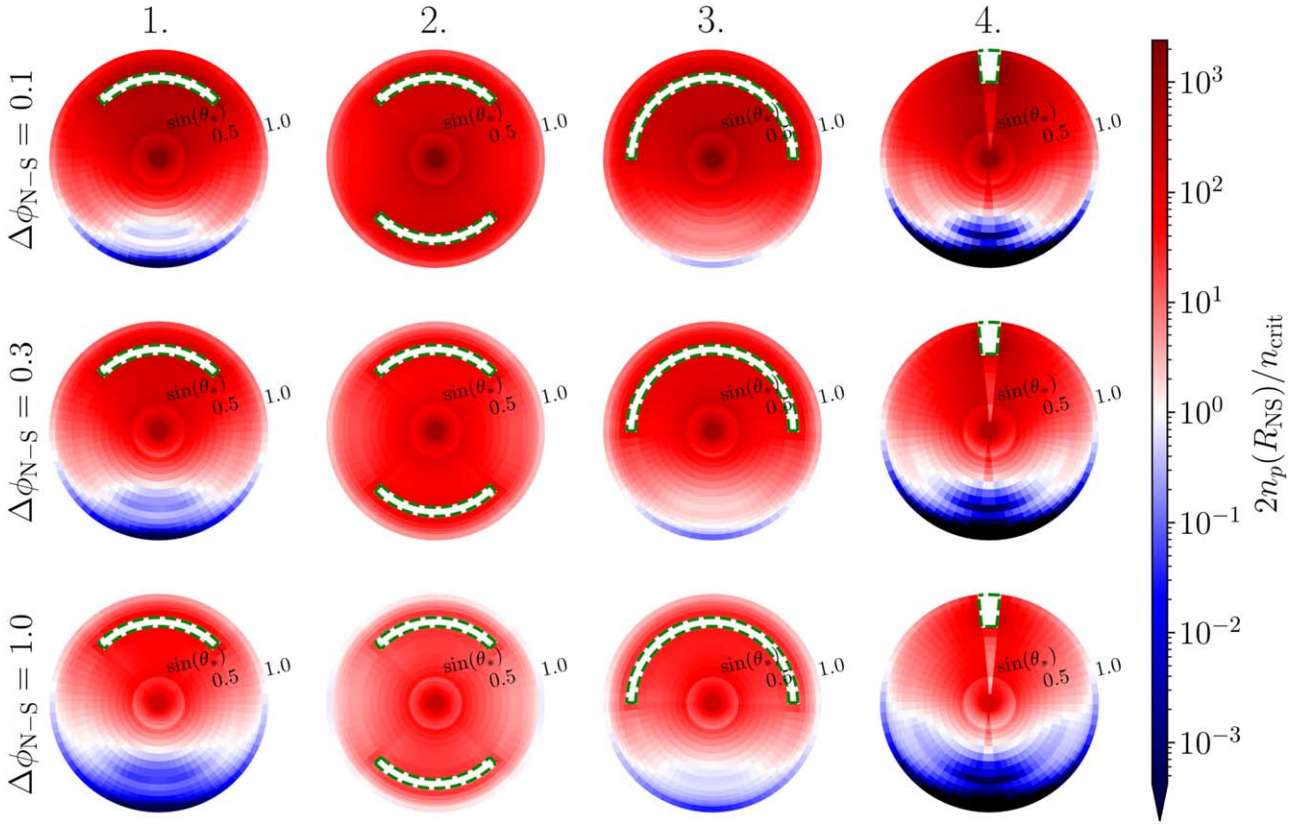

Figure 10. Comparison of the plasma density created by nonlocal pair creation, $\gamma + \gamma \rightarrow e^+ + e^-$, to the critical plasma density that is needed to support a global magnetospheric twist of angle $\Delta\phi_{\rm N-S}$ (Equation (24)). The result is shown for a range of twist angles; a twist angle $\Delta\phi_{\rm N-S} = 1$ corresponds to a substantial increase in spindown rate, by a factor $\sim$10 (C. Thompson et al. 2002).

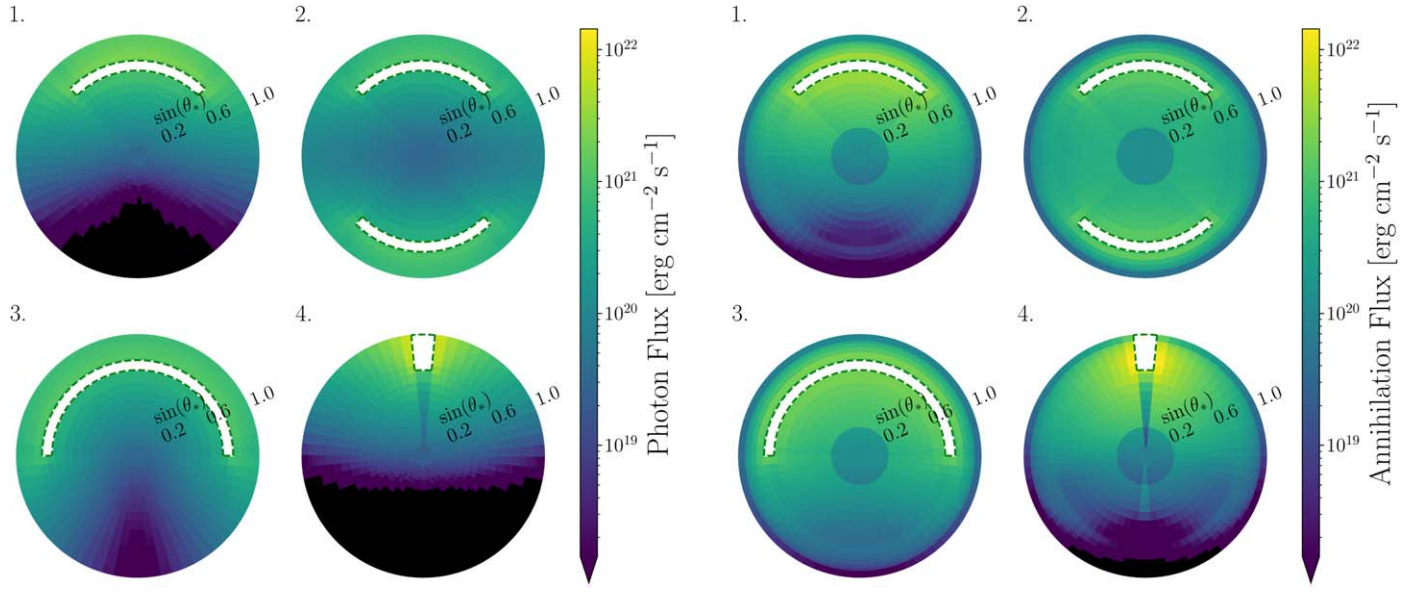

Figure 11. Left panel: surface energy flux of X-rays and gamma-rays hitting the star, multiplied by 0.5 to estimate the effects of reflection. Right panel: net energy flux of electron–positron pairs absorbed and annihilating in the stellar atmosphere (one-third of those impacting the surface; see Section 2.3.2). Plots show the projection along a magnetic polar axis. Fluxes are corrected for the gravitational redshift from the stellar surface to infinity.

energy fluxes in the right panel. (The effective temperature is larger by a factor $2^{1/4}$ than plotted if one allows only for re-radiation into the O-mode.)

We have not attempted to model the frequency distribution of the radiation re-emitted from the surface, comprising photons emitted directly from positron annihilation or resulting from partial thermal equilibration with the atmosphere. Following the discussion in Section 2.3.2, most of the annihilation radiation is concentrated at an O-mode scattering depth less than unity (Equation (13)). When the magnetospheric O-mode depth is low, a significant part of the radiation re-emitted in the X-ray band will therefore follow the same

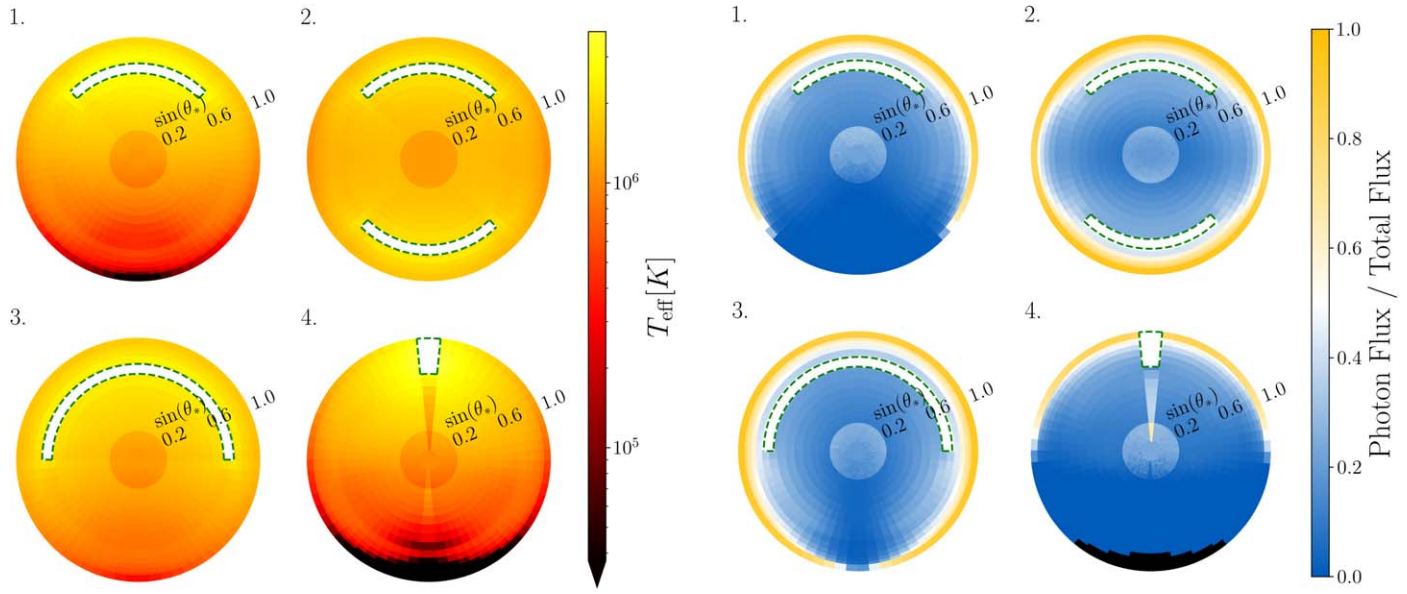

Figure 12. Left panel: surface effective temperature $T_{\rm eff}$ computed from the sum of absorbed radiation and annihilation energy fluxes in Figure 4, and neglecting the contribution of internal heating. Right panel: energy absorbed from photon impact relative to total energy absorbed. Yellow (blue) marks parts of the surface where annihilation (radiation) heating dominates.

annihilation bremsstrahlung spectrum as the primary gamma-ray emitting arcades.

6.4. Resonant Scattering Corona

An outflow of transrelativistic $e^{\pm}$ near the pole of a magnetar will scatter X-ray photons emitted closer to the star. The dominant contribution to the scattering opacity comes from the electron cyclotron resonance. For photons in the 1−10 keV range, this resonance is significantly displaced from the surface of the star (see Equation (17)). To gauge the impact of cyclotron scattering, we consider the interaction near the magnetic pole, where photons and $e^{\pm}$ move nearly radially.

The $e^{\pm}$ feel such a strong drag force that their motion is tied to the angular dispersion of the photons (C. Thompson 2008a; A. M. Beloborodov 2013b); we approximate their motion as cold with speed βc. The position of the resonance is obtained from Equation (17) in terms of the Doppler-shifted photon frequency $\omega' = \gamma(1-\beta)\omega$ and the polar magnetic field $B_{\rm pole}$. The optical depth is obtained by integrating over the cross section $\sigma_{\rm res} = (2\pi^2 e^2/m_e c)\delta(\omega' - \omega_{ce})$, giving

$$\begin{aligned}\tau_{\rm res} &= \int dr\ (1-\beta) 2 n_p(r)\ \sigma_{\rm res} \\ &= \frac{\pi}{4\alpha_{\rm em}} \frac{(1-\beta)^{2/3}\tau_{\rm T,NS}}{\gamma^{1/3}} \frac{(m_e c^2/\hbar\omega)^{1/3}}{(B_{\rm pole}/B_{\rm Q})^{2/3}} \\ &= 93\ \tau_{\rm T,NS} \frac{({\rm keV}/\hbar\omega)^{1/3}}{(B_{\rm pole}/10\,B_{\rm Q})^{2/3}}. \qquad (\beta = 0.6) \end{aligned} \tag{37}$$

Here, we use the shorthand $\tau_{\rm T,NS} \equiv \sigma_{\rm T} \cdot 2 n_{p,{\rm NS}} R_{\rm NS}$ and apply the radial scalings $n_p(r) = (r/R_{\rm NS})^{-3} n_{p,{\rm NS}}$ and $\omega_{ce} \propto r^{-3}$.

The result is plotted in the top row of Figure 13, focusing on the circular zone surrounding the pole in Figure 9 where the pair density is depleted due to outflow. For the adopted gamma-ray luminosity of $10^{35}\,{\rm erg\,s^{-1}}$, the optical depth reaches $\tau_{\rm res} \sim 5-10$ along much of this field bundle. This shows that $L_0 \sim 10^{35}$ erg s^{-1} is an approximate lower bound to the gamma-ray luminosity of a magnetar that seeds enough transrelativistic pairs to significantly rescatter X-rays around the kiloelectronvolt blackbody peak.

The pair density is distributed inhomogeneously across this extended magnetic field bundle. This inhomogeneous distribution will translate into azimuthal variations in $\tau_{\rm res}$ within the resonant scattering zone. In this way, we obtain a direct connection between azimuthal variation in the yielding profile of the magnetar crust at large distances from the poles, which translate into azimuthal variations in the flux of annihilation radiation in the inner magnetosphere, and thereafter into measurable changes in the pulse profile in the lower-frequency X-ray band.

6.5. Lower Polar Field Strength: 1E 2259+586

When the polar field is reduced from $10\,B_{\rm Q}$ to $4\,B_{\rm Q}$, while fixing L_0, the efficiency of pair creation is reduced by a factor ∼2. This is mainly due to the reduction in the cross section for $\gamma-\gamma$ collisions ($\sigma_{\gamma\gamma} \propto B/B_{\rm Q}$ when $B \gtrsim B_{\rm Q}$), and also due to the tighter kinematic constraints on two-photon pair creation in the weaker field.

Figures 14–16 show the pair density, the ratio of the pair density to the critical density supporting a global twist, and the surface energy flux and temperature for all four arcade models. Comparing with Figures 9, 10, and 12 for the case $B_{\rm pole} = 10\,B_{\rm Q}$, one sees a modest expansion in the size of the zone where n_p is smaller than the critical density that will support a global twist. This effect is most prominent in the gamma-ray shadow opposite the emitting arcades, and is partly compensated for by a reduction in the current density associated with a given global twist angle $\Delta\phi_{\rm N-S}$.

The decreases in pair density and in $B_{\rm pole}$ have opposing effects on the optical depth to electron cyclotron scattering (Equation (37)). As a result, we find $\tau_{\rm res} \sim 5-10$ on much of the polar field bundle reaching radius $r_{\rm res} \sim 15\,R_{\rm NS}$; see the bottom row of Figure 13.

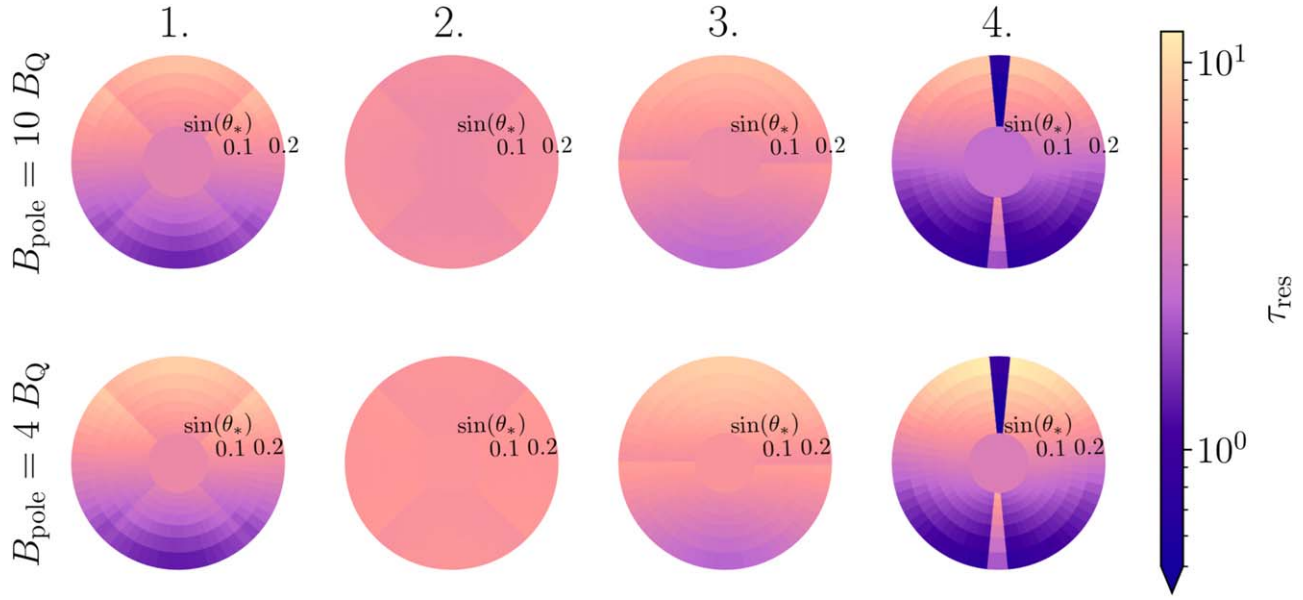

Figure 13. Optical depth $\tau_{\rm res}$ to electron cyclotron scattering, from Equation (37), plotted for each field bundle anchored near the polar cap. Results are presented for (top row) $B_{\rm pole} = 10\ B_{\rm Q}$ and $L_0 = 10^{35}$ erg s^{-1}, and (bottom row) $B_{\rm pole} = 4\ B_{\rm Q}$ and $L_0 = 10^{35}$ erg s^{-1}. The view is the same polar projection as in Figures 9–12, but now focusing on the circular zone near the magnetic axis where dipole field lines reach the resonance radius of Equation (17), and n_p is depleted. (For reference, the central pixel in this plot is now the axial grid cell.) The physical width of the zone plotted grows by a factor $\sim(r_{\rm res}/R_{\rm NS})^{3/2}$ near the scattering radius $r_{\rm res}$.

7. Implications for Magnetar Behavior

The problem posed by magnetar electrodynamics has a few aspects. (1) Where do currents flow outside the star and how smooth is the pattern of crustal shearing? (2) How is $e^{\pm}$ plasma sustained in the magnetosphere and in what kinetic state? (3) How closely tied is the energetically dominant hard X-ray emission of a quiescent magnetar to the processes sustaining the current?

A popular approach to modeling the hard X-ray emission of a magnetar is to posit the acceleration of relativistic charges in parts of the magnetosphere where $B < B_{\rm Q}$. Outflowing charges reaching 150−300 km from the star will resonantly upscatter kiloelectronvolt photons with a hard spectrum (M. G. Baring & A. K. Harding 2007; R. Fernández & C. Thompson 2007). This process has been connected self-consistently to the relativistic double-layer plasma state (A. M. Beloborodov 2013a; Z. Wadiasingh et al. 2018). It is challenging in this picture to explain a rapid increase in hard X-ray output that is *not* accompanied by a prompt surge in the spindown torque. The rapidity of the luminosity increase implies a concentration of the driving crustal motions around the pole.

C. Thompson & A. Kostenko (2020) demonstrated how hard-spectrum X-ray emission follows directly from a state of pair annihilation-creation equilibrium in zones of high current density. These twist zones could form anywhere in the inner magnetosphere. The emission spectrum produced at moderate dissipation rates carries the direct signature of a QED process ($e^{\pm}$ annihilation) operating in magnetic fields above $\sim 10^{14}$ G. We have examined the global consequences of this process, especially for the polar zones that control the spindown torque, radio emission, and emergent X-ray pulse profile.

With this aim, we developed an MC description of nonlocal pair creation around a magnetar. The rate for $\gamma + \gamma \rightarrow e^+ + e^-$ is enhanced by a factor $\sim B/B_{\rm Q}$ in the super-strong magnetic field; the kinematic constraints on $e^{\pm}$ pair creation are also relaxed compared with an unmagnetized vacuum. We consider a range of dissipative structures anchored at intermediate latitudes, away from the magnetic poles, and include the expansion in gamma-ray exposure due to gravitational lensing. These calculations provide a benchmark demonstrating the sort of resolution required to represent the physics in a fully three-dimensional and general relativistic particle-in-cell simulation.

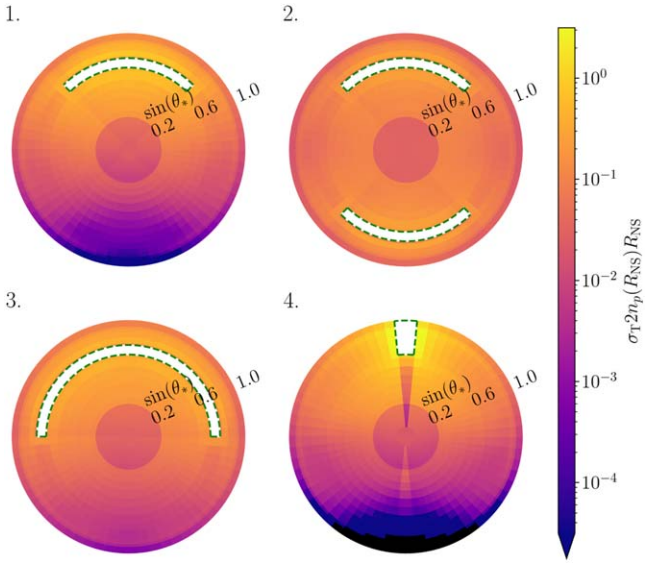

Figure 14. Equilibrium density $n_{e^+} + n_{e^-}$ at the surface of the star, as in Figure 9, but now for a lower polar field 4 $B_{\rm Q}$ and higher luminosity $L_0 = 10^{35}$ erg s^{-1}.

Our calculations apply to a source like 1E 2259+586 with a hard X-ray continuum of moderate intensity, and a lower optical depth to gamma-ray collisions than the brightest persistent magnetars. Even when the measured 15−60 keV flux is around 10^{34} erg s^{-1}, corresponding to a bolometric gamma-ray flux near 10^{35} erg s^{-1}, the pair creation rate in the polar zones is easily high enough to support a magnetic twist $\Delta\phi_{\rm N\text{–}S} \sim 0.1-1$ radians. Enough particles are generated to short out the relativistic double-layer structure that would form

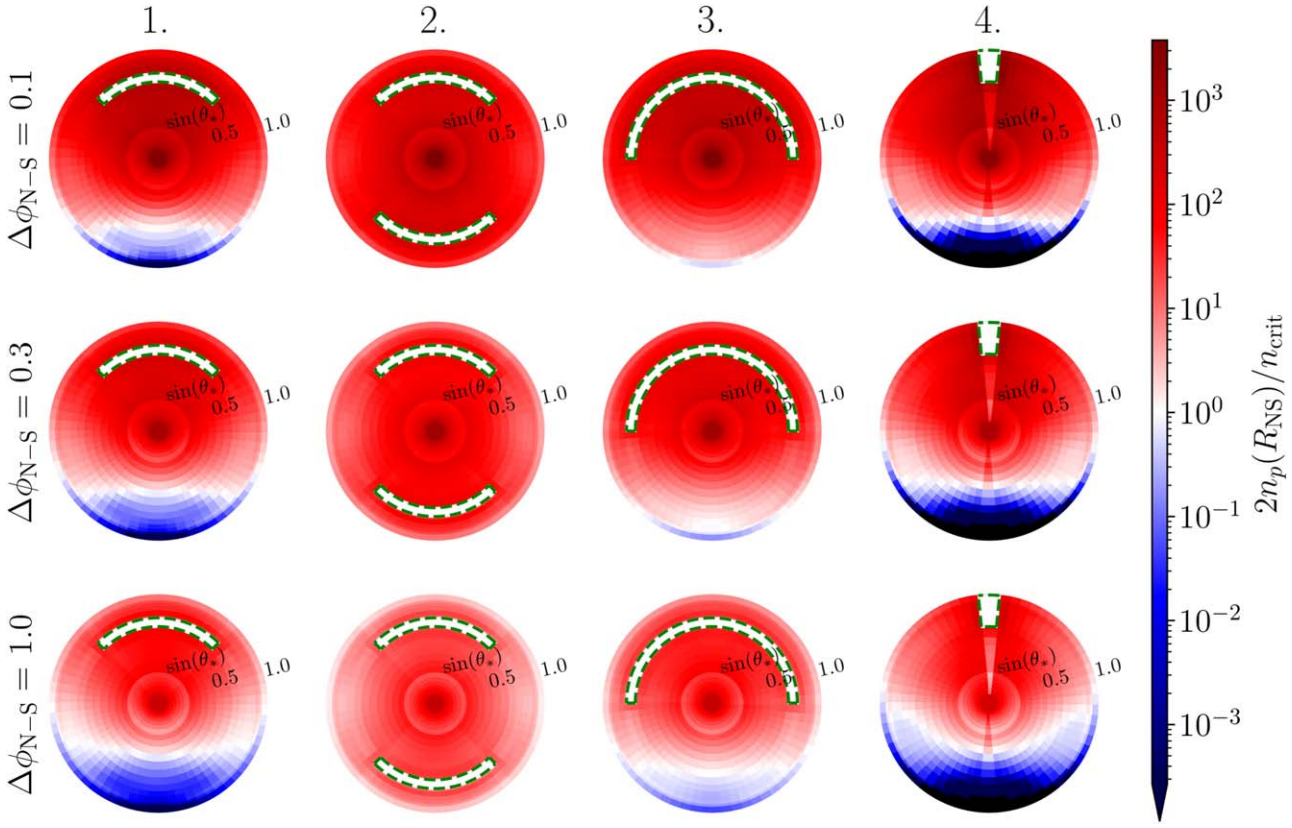

Figure 15. Comparison of the plasma density to the critical density needed to support a global magnetospheric twist, as in Figure 10, but now for a lower polar field 4 $B_{\rm Q}$ and luminosity $L_0 = 10^{35}$ erg s^{-1}.

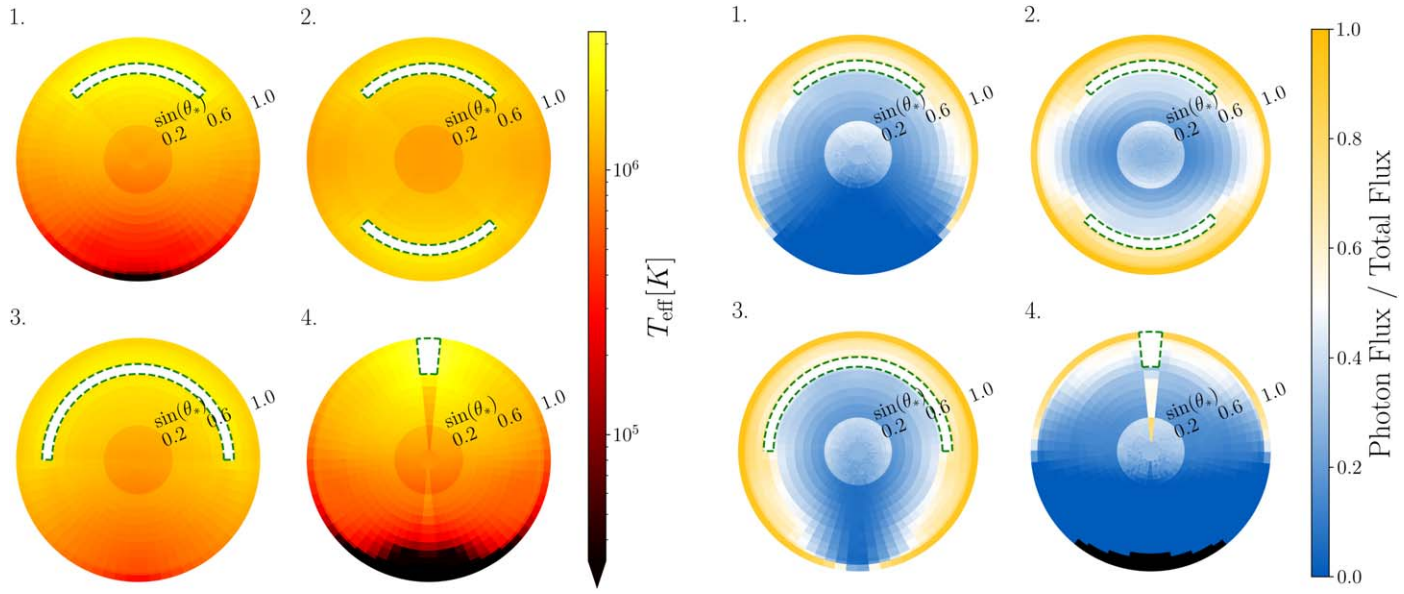

Figure 16. Surface effective temperature (left panel) and comparison of absorbed photon and annihilation heat fluxes (right panel), as in Figure 12, but now for a lower polar field 4 $B_{\rm Q}$ and luminosity 10^{35} erg s^{-1}.

if the magnetosphere were more smoothly twisted (A. M. Beloborodov & C. Thompson 2007).

More generally, the quiescent magnetar 1E 2259+586 can be viewed as a Rosetta Stone for understanding the electrodynamics of magnetars and their broadband electromagnetic emission. Its hard 15−60 keV spectrum is consistent with pair annihilation in a magnetic field around $B_{\rm Q}$ (see Figure 3 of C. Thompson & A. Kostenko 2020). By contrast, the spin history of 1E 2259+586 is consistent with weak twisting of the polar magnetic field. Its overall behavior fits well with our inference that hard X-ray emission and associated optical-IR plasma emission originate in the inner magnetosphere.

We next summarize some implications of the MC results presented here.

7.1. Predictions and Implications for Magnetar Physics

1. *Gamma-ray spectrum.* The X-ray continuum measured up to 50−100 keV is predicted to extend up to ∼0.5−1 MeV, but then cut off sharply. (See the sample spectra in Figure 14 of C. Thompson & A. Kostenko 2020.) This continuum bears a direct imprint of QED processes operating in super-Schwinger magnetic fields. In magnetic fields stronger than B_Q, the two-photon decay of an electron–positron pair becomes a soft-photon correction to single-photon decay, with a flat photon spectrum.

2. *Pseudofaults.* Zones of concentrated magnetospheric shear, which host collisional pair plasma, are connected to narrow shear zones of a subkilometer width in the solid crust. Magnetar outbursts provide strong evidence for such structures. The durations of most short X-ray bursts are comparable to the time for solid stresses to adjust globally in the crust (E. Göğüş et al. 2001), even while high-temperature post-burst afterglow is concentrated in a tiny fraction of the stellar surface (e.g., P. M. Woods et al. 2004). These structures have also been shown to arise in a global elastic-plastic-thermal model of the magnetar crust (C. Thompson et al. 2017).

3. *X-ray reprocessing by cyclotron scattering.* Nonlocal $e^{\pm}$ creation in the polar zones has significant implications for the emergent X-ray polarization and X-ray pulse profiles. The flux of transrelativistic pairs moving out beyond ∼15−30 stellar radii is high enough to generate an optical depth 3−30 to electron cyclotron scattering (Figure 13), even for a gamma-ray luminosity $L_0 = 10^{35}$ erg s^{-1} adjusted to the modest nonthermal output of 1E 2259+586. The inhomogeneity of the pair creation profile above the polar cap translates into axial variations in the optical depth to resonant scattering, which are a source of pulsations.

At the same time, the pairs that resonantly scatter kiloelectronvolt photons will add negligibly to the energy of the scattered X-rays. The kinetic energy carried by the pairs within a polar angle $\theta_\star \sim (r_{\rm res}/R_{\rm NS})^{-1/2} = 0.2\,(B_{\rm pole}/10\,B_Q)^{-1/6}(\hbar\omega/{\rm keV})^{1/6}$ is

$$L_{\rm kin} = \pi\theta_\star^2 R_{\rm NS}^2 \cdot 2n_{p,{\rm NS}}(\gamma-1)\beta m_e c^3 \sim 9\times10^{31}\left(\frac{\tau_{\rm res}}{10}\right)\left(\frac{\hbar\omega}{\rm keV}\right)^{2/3}\left(\frac{B_{\rm pole}}{10\,B_Q}\right)^{1/3}{\rm erg\ s^{-1}}. \quad (38)$$

A background polar magnetic twist $\Delta\phi_{\rm N-S}$ will enforce a small differential drift of the e^+ and e^-, with a speed $\Delta\beta_{+-} \sim n_{\rm crit}/n_p$, where $n_{\rm crit} = J/2e\beta c$ is given by Equation (24). This differential drift causes an average frequency shift $\sim\Delta\beta_{+-}^2$ per scattering, thereby driving a fractional increase $\sim\tau_{\rm res}\Delta\beta_{+-}^2 \propto \tau_{\rm res}^{-1}$ in the X-ray power. This change is modest even for large twist, given that $\Delta\beta_{+-} \sim \Delta\phi_{\rm N-S}/\tau_{\rm res}$ in the resonant scattering zone.

As a result, the transrelativistic pairs are expected to have a weaker effect on the emergent X-ray spectrum than in the calculations of R. Fernández & C. Thompson (2007) and L. Nobili et al. (2008), where the particle density was tied to the critical density needed to support the local magnetic twist, and in the models of A. M. Beloborodov (2013a) and Z. Wadiasingh et al. (2018), where the pairs are injected relativistically above the polar cap and are the main energy source for the hard X-ray continuum.

4. *Emergent X-ray polarization.* A significant flux of E-mode photons will be generated by scattering from the O-mode. (The gyrating electron couples to both polarization modes, the coupling to the O-mode being suppressed by a factor $(\cos\theta_{kB}^O)^2 = (\hat{k}^O\cdot\hat{B})^2$ compared with the coupling to the E-mode.) In fact, at the high optical depths considered, a simple argument suggests that the net polarization is significantly reduced. In contrast with the case of $e^{\pm}$ drift at low optical depth in a fixed central radiation field (A. M. Beloborodov 2013b), the photon flow must come into approximate alignment with the magnetic field within the resonance. We balance the rates of scattering from O to E and E to O and make use of the cross sections (A. K. Harding & D. Lai 2006) $d\sigma_{\rm res}^{O\to E}/d\Omega_E = (\cos\theta_{kB}^O)^2(3\pi^2 r_e c/8\pi)\delta(\omega'-\omega_{ce})$ and $d\sigma_{\rm res}^{E\to O}/d\Omega_O = (\cos\theta_{kB}^O)^2(3\pi^2 r_e c/8\pi)\delta(\omega'-\omega_{ce})$. This gives $n_E = n_O$ in each angular direction at high optical depth with multiple scattering. Photons of both polarization modes scatter at the same rate when propagating along $\boldsymbol{B}$. There is an interesting potential connection here with measurements of 10%–30% net polarization in the 2–4 keV band by IXPE in the three magnetars 4U 0142+61, 1E 2259+586, and 1E 1841−045 (R. Taverna et al. 2022; J. Heyl et al. 2024; M. Rigoselli et al. 2025).

5. *Surface composition.* The energies of the particles hitting the magnetar surface (both pairs and gamma-rays) are cut off sharply above ∼1 MeV. Knockout of neutrons and protons out of heavy nuclei requires higher energies of at least 15–20 MeV (S. S. Dietrich & B. L. Berman 1988). As a result, a heavy atmospheric composition and a condensed state (D. Lai 2001) are more plausibly maintained when the plasma around the magnetar is collisional and transrelativistic, than when it is composed of relativistic $e^{\pm}$ streaming with energies of hundreds of megaelectronvolts (A. M. Beloborodov & C. Thompson 2007).

6. *Correlation between hard X-ray and IR emission.* The enhanced IR-optical emission of magnetars is naturally connected with the collisional zones of hard X-ray emitting plasma, where the plasma frequency lies in this band (C. Thompson & A. Kostenko 2020). Significant correlations between changes in hard X-ray and IR output should therefore be present; there is already evidence for such a correlation in softer X-ray bands following the 2003 outburst of 1E 2259+586 (C. R. Tam et al. 2004). The rapid and persistent changes that are detected in the magnetar radio pulse profile (e.g., Z.-P. Huang et al. 2023) are consistent with the radio emission being concentrated much closer to the separatrix between open and closed magnetic field lines (C. Thompson 2008b).

7.2. Higher Luminosity and Stronger Magnetic Field

Some magnetars emit 15−60 keV radiation with a luminosity 100 times higher than 1E 2259+586: these include the most active burst sources SGR 1806−20 and SGR 1900+14 and also the less active anomalous X-ray pulsar 1E 1841−045 (T. Enoto et al. 2017). The 15−60 keV X-ray spectra are slightly softer ($\Gamma_X \simeq -1$) in the latter two sources, consistent with annihilation bremsstrahlung in magnetic fields stronger than $4\,B_Q$. Indeed, the polar magnetic fields inferred from spindown are $>10^{15}$ G in all three sources. Much of the stellar surface may be threaded by fields approaching $100\,B_Q \sim 5\times10^{15}$ G. (The case for high magnetization is strongest for SGR 1806−20, which emitted a gamma-ray flare in 2004 carrying an energy ∼5 × 10^{46} erg, approaching the total energy in a 10^{15} G dipole magnetic field; K. Hurley et al. 2005; T. Terasawa et al. 2005.)

In these luminous and strongly magnetized sources, the optical depth to $\gamma-\gamma$ collisions is high enough that most gamma-rays of energy $\gtrsim m_e c^2$ emitted from the twist zones will

be absorbed over a fraction of the stellar radius. (A hint of this effect is seen in our narrow wedge model 4 with $B_{\rm pole} = 10\,B_{\rm Q}$; see Figure 9.) The most energetic annihilation bremsstrahlung photons (with frequencies just below the threshold $\omega_{1\gamma}$ for direct pair conversion) experience an additional resonant enhancement in their cross section for electron scattering.[5] In this scattering channel, the final-state photon is usually above threshold for immediate conversion to a pair, yielding $\gamma + e^{\pm} \rightarrow e^{+} + e^{-} + e^{\pm}$ (A. Kostenko & C. Thompson 2018). Incorporating this effect accurately in an MC calculation requires angle-dependent frequency binning, which is challenging in a nonuniform magnetic field.

The strong magnetic field acts as a capacious reservoir for pairs, with the rate of two-photon annihilation being suppressed by a factor $(B/B_{\rm Q})^{-1}$. In annihilation-creation equilibrium, the ratio of pair and photon densities is given by Equation (9). The rate of emission of gamma-rays with energy $>m_e c^2$ in our adopted spectrum of Equation (33) is $0.24 L_0/m_e c^2$. Balancing isotropic emission from arcade structures with area A with annihilation in nearby magnetic field, one obtains an equilibrium pair density $\sigma_{\rm T} n_p R_{\rm NS} = 100\,B_{15}(L_0/4\times10^{36}\ {\rm erg\ s^{-1}})(A/4\pi R_{\rm NS}^2)^{-1}$. A similar result is obtained by balancing with surface annihilation, which is also limited by outward radiation pressure on the downward moving pairs. Given such a high pair density, the flux of photons with energies above $m_e c^2$ is rapidly degraded by electron recoil and pair conversion. The density and temperature of the pairs must therefore drop rapidly with distance from the surface of the current-carrying twist zone.

It should be emphasized that the flat bremsstrahlung number spectrum is preserved by multiple Compton scattering by warm electrons: the same spectral slope $dn_\gamma/d\omega \propto \omega^{-1}$ corresponds to a uniform flux of photons upward in frequency space (A. S. Kompaneets 1957). When the pairs are continuously heated (as in a zone of high current density), the formation of a Wien peak is avoided because photons upscattered to an energy $\sim m_e c^2$ are efficiently converted back to pairs, with a large ratio $n_p/n_\gamma(\hbar\omega > m_e c^2)$. A full test of the emitted X-ray spectrum requires a modification of the leaky box MC simulation of C. Thompson & A. Kostenko (2020) to include (i) inhomogeneous currents and magnetic fields; (ii) collisions between $e^{\pm}$ mediated by one-photon annihilation; and (iii) self-consistent solution of the Maxwell equation to obtain the resistive electric field. A parallel effort is required to model the radiative output of positron annihilation in the magnetar atmosphere, including backscattering of warm positrons and electrons (both by one-photon annihlation and ion collision), bremsstrahlung photon emission, and multiple electron-photon scattering (A. Kostenko 2020).

[5] This resonance involves a vertex between the incoming electron, a virtual positron, and the final-state photon (A. Kostenko & C. Thompson 2018).

Acknowledgments

This research was supported by NSERC grant RGPIN-2023-04612 and by the Simons Foundation grant MP-SCMPS-00001470-08.

Appendix
Distribution of Pair Creation with Photon Energy

Here we tabulate how $e^{\pm}$ pair creation is distributed with respect to the energy carried by the more energetic photon involved in each photon collision. Figure 17 shows this quantity as normalized by the emission rate of the more energetic seed photon. We excise the contribution to $\dot{N}_{\gamma\gamma\rightarrow e^+e^-}$ when this ratio is larger than unity in arcade models 1–3, so as to avoid overcounting.

Photons of energy $\gtrsim 2\,m_e c^2$ can convert to a pair by colliding with a wide range of soft photons, with a cross section in the strong magnetic field scaling with the soft photon energy as ω^{-3} (Equation (6). For the MC runs with $B_{\rm pole} = 10\,B_{\rm Q}$, in the top row of Figure 17, the top 14–17 energy bins are removed, lowering the overall pair production rate by $\sim$90%. For the models with $B_{\rm pole} = 4\,B_{\rm Q}$, in the bottom row of Figure 17, only the top 13 energy bins are removed, reducing the pair production rate by $\sim$80%. Photons of energy $\gtrsim 2\,m_e c^2$ carry $<$10% of the annihilation energy; they convert rapidly enough to pairs that their energy is effectively transferred to lower-energy photons by repeated annihilations.

In model 4, we find that almost one-half of the pair creation is concentrated in the set of cells adjacent to the arcade (Table 3). The energy deposited in these pairs is mainly re-released by magnetospheric annihilation, thereby expanding the effective emitting surface and sustaining the rate of pair creation in more distant cells.

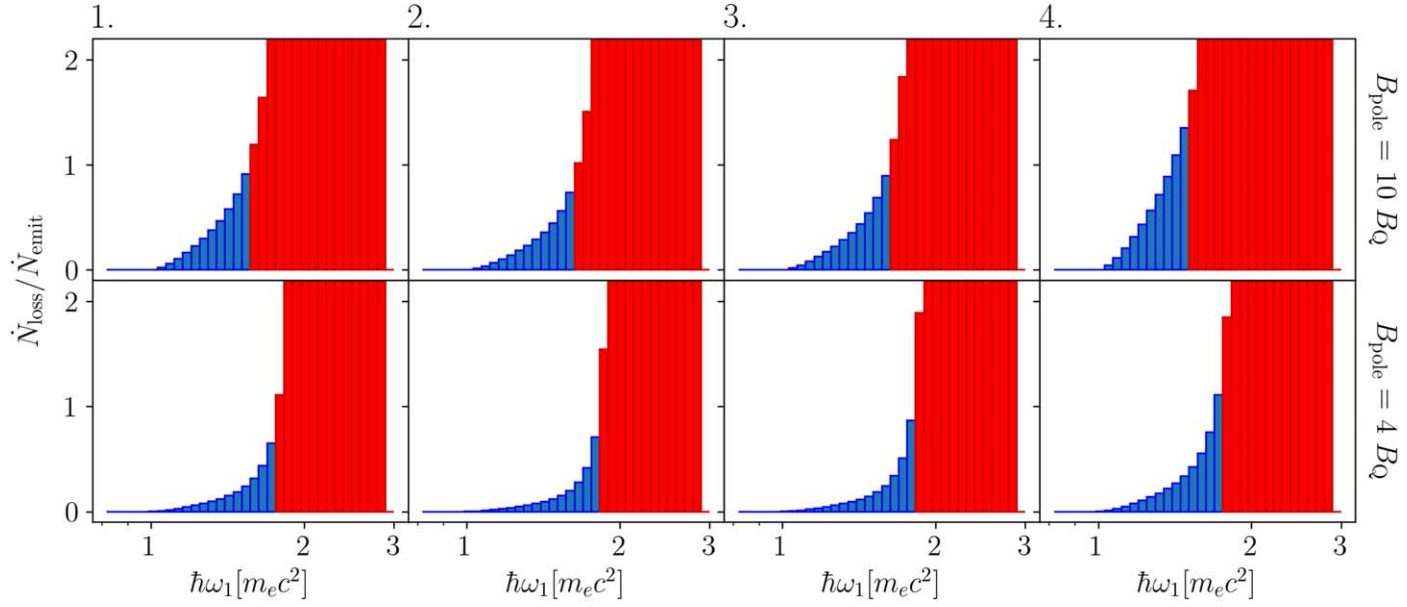

Figure 17. Ratio of the rate of photon consumption to photon emission rate, as binned by the energy of the more energetic photon in each collision event. Results are presented for (top row) $B_{\rm pole} = 10\ B_{\rm Q}$ and (bottom row) $B_{\rm pole} = 4\ B_{\rm Q}$, both with $L_0 = 10^{35}$ erg s^{-1}. We choose a cutoff on the upper photon energy such that this ratio does not exceed 1 for arcade models 1–3. As result, the red bins do not contribute to the tabulated pair creation rate, corresponding to all photons of energy $\gtrsim(1.5-1.6)\ m_e c^2$. Note that the adopted emission energy spectrum $dL_\gamma/d\ln\omega$ peaks at $\hbar\omega \simeq m_e c^2$ and is smaller by a factor 0.1 at $2m_e c^2$. In the case of arcade model 4, almost half of the pair creation is localized in the set of cells next to the emitting arcade, indicating an expansion of the emission surface of the pair-creating gamma-rays (see Table 3). We adopt a limiting ratio 1.5 for model 4.

ORCID iDs

Christopher Thompson https://orcid.org/0000-0003-4305-5653

References

Adler, S. L. 1971, AnPhy, 67, 599
Archibald, R. F., Kaspi, V. M., Ng, C.-Y., et al. 2015, ApJ, 800, 33
Baring, M. G., & Harding, A. K. 2007, Ap&SS, 308, 109
Beloborodov, A. M. 2009, ApJ, 703, 1044
Beloborodov, A. M. 2013a, ApJ, 762, 13
Beloborodov, A. M. 2013b, ApJ, 777, 114
Beloborodov, A. M., & Thompson, C. 2007, ApJ, 657, 967
Berestetskii, V. B., Lifshitz, E. M., & Pitaevskii, V. .B. 1982, Quantum Electrodynamics (Oxford: Pergamon)
Bochenek, C. D., Ravi, V., Belov, K. V., et al. 2020, Natur, 587, 59
Breit, G., & Wheeler, J. A. 1934, PhRv, 46, 1087
Burns, E., Svinkin, D., Hurley, K., et al. 2021, ApJL, 907, L28
Camilo, F., Ransom, S. M., Halpern, J. P., et al. 2006, Natur, 442, 892
Camilo, F., Ransom, S. M., Halpern, J. P., et al. 2007, ApJL, 666, L93
Chen, A. Y., & Beloborodov, A. M. 2017, ApJ, 844, 133
CHIME/FRB Collaboration, Andersen, B. C., Bandura, K. M., et al. 2020, Natur, 587, 54
Coe, M. J., Jones, L. R., & Lehto, H. 1994, MNRAS, 270, 178
Daugherty, J. K., & Bussard, R. W. 1980, ApJ, 238, 296
den Hartog, P. R., Kuiper, L., Hermsen, W., et al. 2008a, A&A, 489, 245
den Hartog, P. R., Kuiper, L., & Hermsen, W. 2008b, A&A, 489, 263
Dib, R., & Kaspi, V. M. 2014, ApJ, 784, 37
Dietrich, S. S., & Berman, B. L. 1988, ADNDT, 38, 199
Eichler, D., Gedalin, M., & Lyubarsky, Y. 2002, ApJL, 578, L121
Enoto, T., Shibata, S., Kitaguchi, T., et al. 2017, ApJS, 231, 8
Fahlman, G. G., & Gregory, P. C. 1981, Natur, 293, 202
Fernández, R., & Thompson, C. 2007, ApJ, 660, 615
Gonthier, P. L., Baring, M. G., Eiles, M. T., et al. 2014, PhRvD, 90, 043014
Göğüş, E., Kouveliotou, C., Woods, P. M., et al. 2001, ApJ, 558, 228
Götz, D., Mereghetti, S., Tiengo, A., et al. 2006, A&A, 449, L31
Harding, A. K., Contopoulos, I., & Kazanas, D. 1999, ApJL, 525, L125
Harding, A. K., & Lai, D. 2006, RPPh, 69, 2631
Heyl, J., Taverna, R., Turolla, R., et al. 2024, MNRAS, 527, 12219
Huang, Z.-P., Yan, Z., Shen, Z.-Q., et al. 2023, ApJ, 956, 93
Hulleman, F., Tennant, A. F., van Kerkwijk, M. H., et al. 2001, ApJL, 563, L49
Hurley, K., Boggs, S. E., Smith, D. M., et al. 2005, Natur, 434, 1098
Kaspi, V. M., & Beloborodov, A. M. 2017, ARA&A, 55, 261
Kompaneets, A. S. 1957, JETP, 4, 730
Kostenko, A. 2020, Ph.D. thesis, Univ. Toronto
Kostenko, A., & Thompson, C. 2018, ApJ, 869, 44
Kostenko, A., & Thompson, C. 2019, ApJ, 875, 23
Kozlenkov, A. A., & Mitrofanov, I. G. 1986, JETP, 64, 1173
Kuiper, L., Hermsen, W., den Hartog, P. R., et al. 2006, ApJ, 645, 556
Lai, D. 2001, RvMP, 73, 629
Landau, L. D., & Lifshitz, E. M. 1975, The Classical Theory of Fields (Oxford: Pergamon)
Levin, L., Bailes, M., Bates, S., et al. 2010, ApJL, 721, L33
Lyutikov, M. 2006, MNRAS, 367, 1594
Mahlmann, J. F., Philippov, A. A., Mewes, V., et al. 2023, ApJL, 947, L34
Nobili, L., Turolla, R., & Zane, S. 2008, MNRAS, 386, 1527
Parfrey, K., Beloborodov, A. M., & Hui, L. 2012, ApJL, 754, L12
Pavlov, G. G., & Yakovlev, D. G. 1976, JETP, 43, 389
Petroff, E., Hessels, J. W. T., & Lorimer, D. R. 2022, A&ARv, 30, 2
Rigoselli, M., Taverna, R., Mereghetti, S., et al. 2025, ApJL, 985, L34
Tam, C. R., Kaspi, V. M., van Kerkwijk, M. H., et al. 2004, ApJL, 617, L53
Taverna, R., Turolla, R., Muleri, F., et al. 2022, Sci, 378, 646
Terasawa, T., Tanaka, Y. T., Takei, Y., et al. 2005, Natur, 434, 1110
Thompson, C. 2008a, ApJ, 688, 499
Thompson, C. 2008b, ApJ, 688, 1258
Thompson, C., & Blaes, O. 1998, PhRvD, 57, 3219
Thompson, C., & Duncan, R. C. 1995, MNRAS, 275, 255
Thompson, C., & Kostenko, A. 2020, ApJ, 904, 184
Thompson, C., Lyutikov, M., & Kulkarni, S. R. 2002, ApJ, 574, 332
Thompson, C., Yang, H., & Ortiz, N. 2017, ApJ, 841, 54
Turolla, R., Taverna, R., Israel, G. L., et al. 2023, ApJ, 954, 88
Vogel, J. K., Hascoët, R., Kaspi, V. M., et al. 2014, ApJ, 789, 75
Wadiasingh, Z., Baring, M. G., Gonthier, P. L., et al. 2018, ApJ, 854, 98
Woods, P. M., Kaspi, V. M., Thompson, C., et al. 2004, ApJ, 605, 378
Woods, P. M., Kouveliotou, C., Göğüş, E., et al. 2001, ApJ, 552, 748
Wunner, G. 1979, PhRvL, 42, 79
Zhang, B. 2023, RvMP, 95, 035005